Adjoint-based optimization of the actuator velocity profile in an inkjet print head

Petr V. Kungurtsev[a], Matthew P. Juniper[a,*]

[a]*Department of Engineering, University of Cambridge, Trumpington Street, Cambridge CB2 1PZ, UK*

Abstract

We consider the thermo-viscous acoustic flow inside the narrow channel and nozzle of an inkjet print head. We define a cost function to be the sum of the acoustic energy in the channel and the surface energy of the spherical cap of ink at the end of the nozzle. We derive the adjoint equations and obtain the sensitivity of this cost function to boundary forcing from the piezo-electric actuator opposite the nozzle. We use this forcing to eliminate residual oscillations after a droplet is ejected. We use a gradient-based optimization algorithm to find the time-varying boundary forcing that minimizes the cost function at various final times and for geometries with increasing complexity. For all geometries, the actuator first extracts fluid so that the ink/air interface becomes flat. This unavoidably sends an acoustic wave upstream, which reflects off the inlet manifold. The actuator subsequently moves to absorb this returning wave without reflection. The optimal boundary forcing and the final energy depend on the channel length, the actuator length, the forcing's temporal resolution, and the available optimization time. The minimum time required to dampen residual oscillations is the time taken for waves to travel from the actuator to the inlet and back. For times greater than this, the total energy inside the microchannel can be reduced by a factor of 1000 compared to the uncontrolled case. This method is general and can be applied to other cost functions and initial conditions. Successful application of this method could lead more repeatable droplets at higher ejection frequencies.

Keywords: optimization, adjoint, acoustic, inkjet

1. Introduction

An inkjet print head contains several hundred microchannels, each typically 1 mm in length and 70 μm in width and height (Fig. 1). Each channel feeds a short nozzle, typically 50 μm

*Corresponding author
Email address: mpj1001@cam.ac.uk (Matthew P. Juniper)

in length and 20 μm in diameter. There is a free surface at the end of each nozzle, where the ink meets the air. A droplet is expelled through a nozzle when the piezo-electric actuator in the corresponding channel pushes in one side of the channel by a few nanometres. After this, acoustic oscillations reverberate through the channel until damped by visco-thermal mechanisms, which strongly influence wave propagation inside narrow channels [1, 2]. Ref. [3] contains a detailed review of the process, the challenges, and the open questions in inkjet printing.

Drop-on-demand inkjet printing is widely used for printing paper, packaging, and textiles. It is increasingly used for production of 3D electronic components, MEMS devices, and other applications [4, 5]. Manufacturers would like to increase the droplet ejection frequency, while retaining or improving the reproducibility of the droplets. There is, however, a trade-off between the droplet ejection frequency and the droplet reproducibility. This is because, as the time between ejections decreases, each droplet becomes increasingly affected by the residual oscillations from the previous ejection. Manufacturers therefore try to design print head shapes that passively damp residual oscillations. They also alter the electrical waveforms sent to the print heads microchannels in order to damp residual oscillations with open loop control. These waveforms are currently adjusted by trial and error in extensive experimental campaigns. Our first paper on this subject [6] used adjoint methods in the frequency domain. That paper showed how to optimize the shape of the print head microchannel in order to passively damp residual oscillations. This paper uses adjoint methods in the time domain in order to damp residual oscillations with open loop control by optimizing the actuating waveform: the velocity at the actuator channel wall. The adjoint methods in both papers reveal the physical mechanisms being exploited by the optimization algorithms.

Early studies [7, 8] performed experimental and theoretical analysis of acoustic phenomena inside a drop-on-demand piezoelectric print head. Acoustic motion inside tubes or channels with simple geometries can be successfully approximated using reduced analytical models, such as the narrow channel model [1, 2, 9] and the lumped elements method [10]. For channels with smooth boundaries, the acoustic boundary layer model [11] can be applied. While these models are computationally cheap and useful for initial designs, they can fail to predict performance of print heads with complex geometries. In this paper we impose no restrictions on the channel geometry and solve the full system of thermo-viscous acoustic equations in two dimensions. The method can easily be extended to three dimensions.

The flow in the nozzle, which is short, is typically modelled as incompressible and axisymmetric [12, 13], driven by the pressure [14] or velocity inflow [15] from the channel. Separating

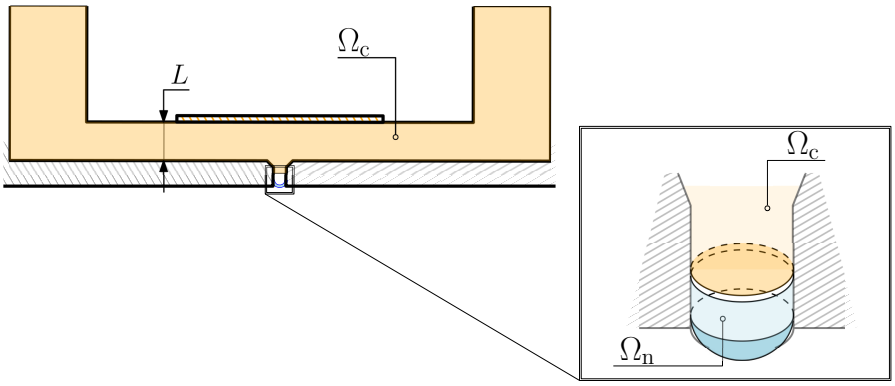

Figure 1: Channel (yellow) and nozzle (blue) domains of a single microchannel within an inkjet print head. In this paper the channel is modelled as 2D planar and the nozzle is modelled as 2D axisymmetric. The piezo-electric actuator sits on the channel wall opposite the nozzle.

the nozzle from the channel allows the two domains to be considered separately and, if analysed numerically, to be discretized independently. In turn this allows the analysis in the nozzle to be focused on droplet formation. Various numerical methods have been proposed to model the free surface development, droplet formation, and pinch-off in inkjet print heads. One-dimensional models of droplet formation [16, 17, 18] and jet break-up [19] have shown good agreement with experiments. The volume of fluid [13] and level-set methods [20, 15] have been successfully applied to compute the position of free surface boundary and droplet formation. In the above methods, the nozzle is assumed always to be filled with fluid. This assumption can be relaxed and the dynamics of the contact line between liquid, solid, and gas can be simulated using a variational approach [14, 21]. In this paper, however, we assume that the nozzle is always filled with fluid and that the fluid/gas interface is a spherical cap. This is a realistic assumption, and it has the advantage that it allows gradients of useful quantities with respect to the inflow conditions to be derived analytically [22, 23]. It could readily be relaxed in subsequent studies, at the expense of extra computational time.

Typical objectives for optimization in inkjet printing are droplet velocity and volume [24], damping of residual oscillations, damping of cross-talk between channels [25, 26], and high frequency jetting [15]. Reducing the nozzle diameter allows jetting at megahertz frequency and smaller droplet size [15]. We do not calculate the waveform of the applied voltage because this would require us to specify and then simulate the piezo-electric actuator, which varies for different devices. We choose instead to focus on the optimization and physical understanding of the fluid motion alone, in order to produce a general result for the motion of the fluid boundary.

With this knowledge, the required voltage can then be found for a given actuator.

The most basic waveform is the unipolar (trapezoidal push in) waveform. This waveform has a number of drawbacks: the volume of the ejected droplets is large, the amplitude of residual reverberations is high, and satellite droplets are formed in addition to the main droplet [27]. Bipolar (trapezoidal push in then trapezoidal pull out) waveforms are used to eliminate satellite droplets [24]. Compared with unipolar and bipolar waveforms [12], the W-shaped waveform type can significantly reduce the volume of the ejected droplet, and eliminate the residual acoustic waves from the last ejection cycle [24]. Droplets formed from complex waveforms are, however, more sensitive to changes in the waveform shape. This means that optimal waveforms become harder to find as the waveform type becomes more complex. Given that waveforms are usually found by trial and error during extensive experiments, this leads to considerable experimental cost as the waveforms become more complex and motivates the more systematic approach in this paper.

Systematic waveform optimization can be approached in several ways. A feed-forward control method [25] can be used to eliminate residual reverberations by flattening the response of the meniscus velocity to the pulse frequency. If numerical models are not accurate enough, or are too computationally expensive to predict the droplet characteristics, then the waveform parameter space can be explored with model-free methods by combining an automated experimental rig with an optimization algorithm. The waveform shape is the experimental input and the droplet characteristics are the experimental output. This method has been used with a genetic algorithm [28] and a swarm-intelligence based technique [10]. Alternatively, a highly efficient instanteneous adjoint-based approach to control the free surface inside the nozzle has been developed by [14], applied to numerical simulations. Our approach is similar, in that it considers a systematic approach to waveform optimization by using adjoint-based optimization. The differences are that this study includes the acoustics in the channel in addition to the flow in the nozzle, but makes an assumption on the spherical shape of the fluid/gas interface.

Adjoint-based optimization can be applied only to numerical simulations. The adjoint methods provide, in a single calculation, the gradient of an objective function with respect to all of the control parameters [29]. This gradient is then used within a gradient-based optimization algorithm in order to converge to a local optimum. This gradient information greatly speeds up optimization. Adjoint-based optimization is faster than non-gradient-based methods when the number of control parameters exceeds the number of objective functions, which is the case here. It has been used in aerodynamics optimization [30], triggering in thermoacoustics [31],

hydrodynamic stability [29] and shape optimization for hydrodynamic stability [32].

In this paper, we start from a moment just after pinch-off of the expelled ligament. We use adjoint-based optimization to optimize a velocity waveform at the actuator in order to reduce residual oscillations to zero within a given time. In order to be effective, this time needs to increase as the length of the printhead microchannel increases so that waves have time to reflect off the opposite end and return [7]. In practice, this time would be the desired period between droplets. Similarly to previous studies we derive different governing equations for the channel and the nozzle. We develop a general approach to couple the channel to the nozzle through the boundary conditions on the surface between the two. We then derive the adjoint of this coupled channel-nozzle system and optimize the velocity waveform at the actuator for various channel shapes and optimization times. In doing so we reveal the physical mechanisms that are exploited in order to reduce the residual oscillations and define the minimum time between droplets. In this paper, we do not consider jetting, droplet coalescence, or entrainment of air bubbles into the nozzle. We also do not consider the actuation cost required to reduce these residual oscillations because this cost is much smaller than the actuation cost of jetting. This is because the jetting pulse creates a large amount of surface area and gives the jet a large kinetic energy, while the residual control movement has to absorb just a small amount of surface energy.

2. Formulation of the Direct Problem

We label the spatial domain $\Omega \subset \mathbb{R}^d$ with boundary $\partial\Omega = \bigcup \Gamma_i \subset \mathbb{R}^{d-1}$, where Γ_i are the labels of sections of the boundary. We label the temporal domain $\mathcal{T} = \{t : 0 < t < t_f\}$, where t_f is the final time. We label the mixed spatio-temporal domain of the problem $\Sigma = (\Omega \times \mathcal{T})$. We define the following scalar products in the spatial, temporal, and mixed domains:

$$[a,b]_\Sigma \equiv \int_{\mathcal{T}} \mathrm{d}t \int_\Omega \mathrm{d}\mathbf{x}\ a^*\ b, \quad \langle a,b\rangle_\Omega \equiv \int_\Omega \mathrm{d}\mathbf{x}\ a^*\ b, \quad \{a,b\}_{\Gamma_i} \equiv \int_{\Gamma_i} \mathrm{d}\mathbf{s}\ a^*\ b. \tag{1}$$

Here * denotes complex conjugation. An integral of a single variable over a domain is equivalent to the corresponding scalar product with $a \equiv 1$, $\langle b\rangle_\Omega \equiv \langle 1, b\rangle_\Omega$.

We split the printhead microchannel into the non-overlapping channel Ω_c and the nozzle Ω_n domains (figure 1). The channel domain consists of the top part of the nozzle and a horizontal channel connected to vertical outlets. The nozzle domain is the bottom part of the nozzle, which includes the liquid/gas interface. The two domains intersect at a (virtual) flat boundary $\Omega_\mathrm{c} \bigcap \Omega_\mathrm{n}$. We couple the flows inside the channel and nozzle domains through velocity and stress boundary conditions on the shared boundary. On the nozzle domain shared boundary $\Gamma_{\mathrm{N-C}} \subset \Omega_\mathrm{n}$, we

prescribe the velocity, which is determined by the flow in the channel domain [13, 33]. On the channel flow shared boundary $\Gamma_{\mathrm{C-N}} \subset \Omega_{\mathrm{c}}$, we prescribe the stress, which is determined by the force applied from the flow in the nozzle.

2.1. Governing equations for the acoustic oscillations in the channel

Using a two-parameter low Mach number asymptotic expansion [6, 34] we separate the compressible Navier–Stokes equations into a stationary ambient state, an incompressible steady flow with no acoustic oscillation, and an acoustic oscillation with no steady flow. Then we consider only the acoustic oscillation with no steady flow. We expand the dimensional flow pressure, velocity and temperature $(P^*, \mathbf{u}^*, T^*)$ in terms of the acoustic Mach number $\epsilon \equiv \|\mathbf{u}^*\| / c_s \ll 1$:

$$P^*(\mathbf{x}, t) = P^b \left(P^{(0)} + \epsilon P \right) + \mathcal{O}\left(\epsilon^2\right), \tag{2a}$$

$$\mathbf{u}^*(\mathbf{x}, t) = c_s \epsilon \mathbf{u} + \mathcal{O}\left(\epsilon^2\right), \tag{2b}$$

$$T^*(\mathbf{x}, t) = T^b \left(T^{(0)} + \epsilon T \right) + \mathcal{O}\left(\epsilon^2\right), \tag{2c}$$

where $P^b P^{(0)}$ is the ambient pressure, $T^b T^{(0)}$ is the ambient temperature, and $(\mathbf{u}, P, T)$ are the nondimensional acoustic velocity, pressure and temperature. We use $\mathcal{Q}_{\mathrm{c}} \equiv (\mathbf{u}, P, T)$ to denote the acoustic state. The speed of sound is set to $c_s = 1000\mathrm{ms}^{-1}$.

The acoustic state $\mathcal{Q}_{\mathrm{c}}$ inside the inkjet channel, $\Sigma_{\mathrm{c}} \equiv (\Omega_{\mathrm{c}} \times \mathcal{T})$, is governed by the linear nondimensional conservation equations for mass, momentum, and energy, with viscous and thermal losses (3). We include the acoustic density $\rho = \gamma_{th} P - T$ and entropy $s = T / (\gamma_{th} - 1) - P$ for convenience:

$$\begin{aligned} &\tfrac{\partial}{\partial t}\rho + \nabla_i u_i = 0, \\ &\tfrac{\partial}{\partial t} u_i + \nabla_i P - \tfrac{1}{Re} \nabla_j \tau_{ij} = 0, \\ &\tfrac{\partial}{\partial t} s - \tfrac{1}{(\gamma_{th}-1) Pe} \Delta T = 0. \end{aligned} \tag{3}$$

The Reynolds and Peclet numbers are based on the speed of sound: $Re = \rho^b L c_s / \mu$, $Pe = \rho^b L c_s c_p / K$, where ρ^b is the fluid density, μ is the dynamic viscosity, K is the thermal conductivity, and c_p is the specific heat at constant pressure. The ratio of specific heats is $\gamma_{th} = 1.017$, which is characteristic of water at 25° [35]. The viscous stress tensor is given by $\tau_{ij} \equiv \boldsymbol{\tau} \circ u = \nabla_j u_i + \nabla_i u_j - 2/3\ \delta_{ij} \nabla_k u_k$.

We rewrite the state equations in matrix form, $\frac{\partial}{\partial t} \mathrm{A}_c \mathcal{Q}_{\mathrm{c}} + \mathrm{B}_c \mathcal{Q}_{\mathrm{c}} = 0$:

$$\frac{\partial}{\partial t} \begin{bmatrix} 1 & 0 & 0 \\ 0 & \gamma & -1 \\ 0 & -1 & \frac{1}{\gamma_{th}-1} \end{bmatrix} \begin{bmatrix} u_i \\ P \\ T \end{bmatrix} + \begin{bmatrix} -\frac{1}{Re}\nabla_j \boldsymbol{\tau} & \nabla_i & 0 \\ \nabla_i & 0 & 0 \\ 0 & 0 & -\frac{\Delta}{(\gamma_{th}-1)Pe} \end{bmatrix} \begin{bmatrix} u_i \\ P \\ T \end{bmatrix} = 0 \tag{4}$$

where either the velocity, $\mathcal{U}_i$, or force, f_i, is prescribed at the boundary. We apply homogeneous no slip and stress-free boundary conditions by setting $\mathcal{U}_i = 0$ on no slip boundaries Γ_{w}, and $f_i = 0$ on stress-free boundaries Γ_{open}:

$$u_i = \mathcal{U}_i \text{ on } \Gamma_{\mathrm{vel}} \text{ or } u_i = 0 \text{ on } \Gamma_{\mathrm{w}},\ \sigma_{ij} n_j = f_i \text{ on } \Gamma_{\mathrm{force}} \text{ or } \sigma_{ij} n_j = 0 \text{ on } \Gamma_{\mathrm{open}}, \tag{5}$$

where $\sigma_{ij} \equiv -P\delta_{ij} + Re^{-1}\tau_{ij}$ is the stress tensor. We apply isothermal boundary condition $T = 0$ on Γ_{w} and Γ_{vel}, and adiabatic boundary conditions $\frac{\partial T}{\partial \mathbf{n}} = 0$ on Γ_{open}.

The total acoustic energy $\mathcal{E}_{\mathrm{ac}}$ [36], volume dissipation, $\mathcal{R}$, and boundary energy flux, $\mathcal{F}$ of the thermoviscous acoustic problem (4) are:

$$\begin{aligned}
\mathcal{E}_{\mathrm{ac}} &= \frac{1}{2}\left\langle \mathcal{Q}_{\mathrm{c}}, \mathrm{A}_c \mathcal{Q}_{\mathrm{c}} \right\rangle_{\Omega_{\mathrm{c}}} = \frac{1}{2}\left(\langle P, \rho \rangle_{\Omega_{\mathrm{c}}} + \langle \mathbf{u}, \mathbf{u} \rangle_{\Omega_{\mathrm{c}}} + \langle T, s \rangle_{\Omega_{\mathrm{c}}} \right), \\
\mathcal{R} &= \left\langle \frac{1}{Re}\tau_{ij}, \nabla_j u_i \right\rangle_{\Omega_{\mathrm{c}}} + \left\langle \frac{1}{(\gamma_{th}-1)Pe} \nabla_j T, \nabla_j T \right\rangle_{\Omega_{\mathrm{c}}}, \\
\mathcal{F} &= \sum_k \mathcal{F}_{\Gamma_{\mathrm{k}}} = \sum_k \left(\{u_i, \sigma_{ij} n_j\}_{\Gamma_k} + \left\{ \frac{1}{(\gamma_{th}-1)Pe} \frac{\partial T}{\partial \mathbf{n}}, T \right\}_{\Gamma_k} \right).
\end{aligned} \tag{6}$$

The volume averaged energy balance is:

$$\frac{d}{dt}\mathcal{E}_{\mathrm{ac}} + \mathcal{R} = \mathcal{F}. \tag{7}$$

The boundary condition at the interface between the channel and the nozzle domains, $\Gamma_{\mathrm{C-N}}$ is derived in section 2.2. The nozzle flow state is defined by the free surface curvature $\hat{\kappa}(t)$ which changes due to the mass flow through the shared boundary as

$$\frac{d\left|\Omega_{\mathrm{n}}(\hat{\kappa})\right|}{d\hat{\kappa}} \frac{d}{dt}\hat{\kappa} = \epsilon \left\{ \mathbf{u} \cdot \mathbf{n} \right\}_{\Gamma_{\mathrm{C-N}}} - \epsilon h_{\mathrm{CL}} \left|\Gamma_{\mathrm{C-N}}\right| \frac{d}{dt}\gamma\hat{\kappa}, \tag{8}$$

where $|\Omega_{\mathrm{n}}(\hat{\kappa})|$ is the volume of the nozzle domain, h_{CL} is the distance between the boundary $\Gamma_{\mathrm{C-N}}$ and the static contact line in the nozzle, and γ is the surface tension coefficient. The channel flow boundary condition on $\Gamma_{\mathrm{C-N}}$ is defined by the free surface curvature $\hat{\kappa}$:

$$\sigma_{ij} n_j = -\gamma\hat{\kappa} n_i - h_{\mathrm{CL}} \left(\partial_t u_i - \frac{1}{Re}\Delta_\Gamma u_i \right) \quad \text{on } \Gamma_{\mathrm{C-N}}.$$

2.2. Reduced order model for the flow in the nozzle

In this paper, we start the optimization process from a moment just after an ejected ligament has pinched off and the fluid-gas interface has returned to the vicinity of the print head. In practice, the time between the end of the jetting pulse and the moment described above would need to be measured experimentally beforehand, and may be different for different jetting pulses.

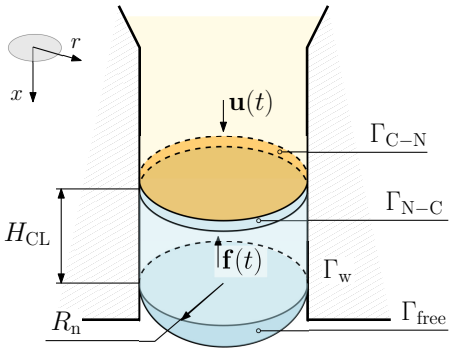

Figure 2: Fluid inside the droplet domain is bounded by the solid walls Γ_{w} and the free surface Γ_{free}, and connects to the channel through $\Gamma_{\mathrm{N-C}}$.

Figure 2 shows the nozzle domain Ω_{n}, which is an axisymmetric tube of radius R_n. The distance between the shared boundary and the multiphase interface at rest (the contact line) is $H_{\mathrm{CL}} = 10\mu$m. Both R_n and H_{CL} are small in comparison to the characteristic channel length, $L = 100\mu$m. The droplet domain is bounded by three types of boundary: the boundary $\Gamma_{\mathrm{N-C}}$ between the nozzle and the channel domains, the no slip wall boundary Γ_{w}, and the moving free surface Γ_{free}. The boundary Γ_{free} is a multiphase interface between the liquid inside the nozzle, the nozzle walls and the outside air. For a typical nozzle radius $R_n = 10\mu$m, fluid density $\rho^b = 10^3$ kg/m^3, and surface tension coefficient $\gamma^* = 50 \times 10^{-3}$ Nm^{-2}, the capillary time scale is $t_\gamma \sim \sqrt{\rho R_n^3/\gamma^*} = 10^{-5}$ s [37, 38]. The acoustic time scale, $t_{ac} \sim L/c_s = 10^{-7}$s, where $c_s \approx 1000$ms^{-1} is the speed of sound. The acoustics therefore occur two orders of magnitude more quickly than the capillary motion, indicating that the capillary motion is quasi-static compared with the acoustic motion. In this paper we model both the acoustic and nozzle flows on the acoustic timescale. We model the boundary condition on $\Gamma_{\mathrm{N-C}}$ as a prescribed velocity, determined by the acoustic oscillations inside the channel. Using the same strategy as for (2), we expand the dimensional nozzle flow variables in terms of the oscillating flow Mach number, $\rho^* \simeq \rho^b \left(1 + \epsilon\rho^{(1)}\right) + \mathcal{O}\left(\epsilon^2\right)$, $\mathbf{u}^* \simeq c_s\epsilon\mathbf{u}^{(1)} + \mathcal{O}\left(\epsilon^2\right)$.

2.2.1. Conservation laws in the nozzle subdomain

We assume that the contact line between the solid, liquid and gas phases is stationary: $\mathbf{u} = 0$ on $\partial\Gamma_{\mathrm{free}} = \Gamma_{\mathrm{free}} \bigcap \Gamma_{\mathrm{w}}$, meaning that the energy of only the liquid-air interface Γ_{free} contributes to the free surface energy. A vector field $\mathbf{w}$ defines the domain deformation due to the movement of the free boundary Γ_{free}. The relationship between $\mathbf{w}$ and $\mathbf{u}$ depends on the type of boundary. On Γ_{w} both the domain and the fluid velocities have zero normal component (9a). On Γ_{free} the

flow velocity and the domain velocity are equal in the normal direction (9b). On $\Gamma_{\mathrm{N-C}}$ there is no deformation (although there is mass flow through this boundary) (9c).

$$\mathbf{w}\cdot\mathbf{n} = \epsilon\mathbf{u}^{(1)}\cdot\mathbf{n} = 0 \quad \text{on} \quad \Gamma_{\mathrm{w}}. \tag{9a}$$

$$\mathbf{w}\cdot\mathbf{n} = \epsilon\mathbf{u}^{(1)}\cdot\mathbf{n} \quad \text{on} \quad \Gamma_{\mathrm{free}}. \tag{9b}$$

$$\mathbf{w}\cdot\mathbf{n} = 0 \quad \text{on} \quad \Gamma_{\mathrm{N-C}}. \tag{9c}$$

The nondimensional nozzle radius and the distance to the contact line are $r_n \equiv R_n/L$ and $h_{\mathrm{CL}} \equiv H_{\mathrm{CL}}/L$. The nondimensional nozzle volume $|\Omega_{\mathrm{n}}(t)|$ is the sum of a static component, $\pi r_n^2 h_{\mathrm{CL}}$, and a time-varying component $\hat{\Omega}_{\mathrm{n}}(t)$, where $|\cdot|$ means surface or volume measure according to the context. A nondimensional effective height of the channel is defined as $h_{\mathrm{n}} \equiv |\Omega_{\mathrm{n}}|/(\pi r_n^2)$. The algebraic relation between the domain volume and the domain deformation, although obvious, can be derived rigorously with the Reynolds transport theorem by considering the time derivative of the volume functional $\mathcal{J} = \langle\phi\rangle_{\Omega}$:

$$\frac{d}{dt}\mathcal{J} = \left\langle \frac{\partial}{\partial t}\phi + div(\phi\mathbf{w}) \right\rangle_{\Omega}. \tag{10}$$

By choosing $\phi \equiv 1$, the functional is the domain volume, $\mathcal{J} = \langle 1\rangle_{\Omega_{\mathrm{n}}} \equiv |\Omega_{\mathrm{n}}|$. After applying the boundary condition (9), the time derivative of the nozzle volume equals the normal flow at the free surface.

$$\frac{d}{dt}|\Omega_{\mathrm{n}}| = \frac{d}{dt}\hat{\Omega}_{\mathrm{n}}(t) = \{\mathbf{w}\cdot\mathbf{n}\}_{\Gamma_{\mathrm{free}}} = \epsilon\left\{\mathbf{u}^{(1)}\cdot\mathbf{n}\right\}_{\Gamma_{\mathrm{free}}}. \tag{11}$$

We apply the Reynolds transport theorem (10) to the continuity equation:

$$\left\langle \frac{\partial\rho}{\partial t} + div(\rho\mathbf{u}) \right\rangle_{\Omega_{\mathrm{n}}} = \frac{d}{dt}\langle\rho\rangle_{\Omega_{\mathrm{n}}} + \langle div(\rho(\mathbf{u}-\mathbf{w}))\rangle_{\Omega_{\mathrm{n}}} = 0.$$

We integrate the divergence term and apply the boundary conditions (9). The nondimensional mass balance equation is

$$\frac{d}{dt}\hat{\Omega}_{\mathrm{n}} = -\epsilon\left\{\mathbf{u}^{(1)}\cdot\mathbf{n}\right\}_{\Gamma_{\mathrm{N-C}}} - \epsilon\frac{d}{dt}\left\langle\rho^{(1)}\right\rangle_{\Omega_{\mathrm{n}}} + \mathcal{O}\left(\epsilon^2\right). \tag{12}$$

The force applied from the free surface to the nozzle flow is proportional to the curvature of the free surface, $\sigma_{ij}^{(1)} n_j = -\gamma\kappa n_i$, where $\gamma \equiv 2\gamma^*/\left(\epsilon\rho^b c_s^2 R_n\right)$ is the nondimensional surface tension coefficient, and $\kappa \equiv \kappa^* R_n/2$ is the nondimensional curvature of the free surface. The pressure drop along the nozzle due to the inertia of the fluid can be estimated as $\rho^b H_{\mathrm{CL}}\omega\|\mathbf{u}\|$, where $\omega \simeq 10^6$ s^{-1} is the characteristic oscillation frequency of the flow. For $\|\mathbf{u}\| = 0.1$ ms^{-1}, the nozzle pressure drop is 10^3 Pa which is equivalent to the pressure of a free surface with curvature

radius $R = 10^{-4}\text{m} = 10R_n$. This shows that the pressure drop along the nozzle is small, but may not be negligible.

We need to account for the kinetic and potential energy of the fluid when the free surface curvature is small. The total energy of the nozzle system $\mathcal{E}_\text{n}$ is a sum of the free surface energy E_free, and kinetic $\mathcal{K}_\text{n}$ and potential $\mathcal{P}_\text{n}$ energy of the nozzle flow: $E_\text{free} = \epsilon^{-1}\frac{r_n}{2}\gamma\left|\Gamma_\text{free}\right|$, $\mathcal{K}_\text{n} = \left\langle \frac{1}{2}\mathbf{u}^{(1)}\cdot\mathbf{u}^{(1)}\right\rangle_{\Omega_\text{n}}$. We assume that the temperature is uniform in the nozzle and neglect the thermal energy, so $\mathcal{P}_\text{n} = \left\langle \frac{1}{2}P^{(1)}\cdot P^{(1)}\right\rangle_{\Omega_\text{n}}$ (and $\rho^{(1)} = P^{(1)}$). The nozzle energy changes due to the viscous dissipation $\mathcal{R}_\text{n} = \frac{1}{Re}\left\langle \tau_{ij}^{(1)}\nabla_j u_i^{(1)}\right\rangle_{\Omega_\text{n}}$ and the energy flux through the shared boundary $\Gamma_{\text{N}-\text{C}}$ are:

$$\frac{d}{dt}\mathcal{E}_\text{n} = \frac{d}{dt}\left(E_\text{free} + \mathcal{K}_\text{n} + \mathcal{P}_\text{n}\right) = -\mathcal{R}_\text{n} + \left\{\sigma_{ij}^{(1)} n_j u_i^{(1)}\right\}_{\Gamma_{\text{N}-\text{C}}}. \tag{13}$$

The time derivative of the free surface energy equals the energy flux through the free surface

$$\frac{d}{dt}E_\text{free} = -\left\{-\gamma\kappa\mathbf{u}^{(1)}\cdot\mathbf{n}\right\}_{\Gamma_\text{free}} = -\gamma\hat{\kappa}\left\{-\mathbf{u}^{(1)}\cdot\mathbf{n}\right\}_{\Gamma_\text{free}}$$

where $\hat{\kappa} \equiv \left\{\kappa\mathbf{u}^{(1)}\cdot\mathbf{n}\right\}_{\Gamma_\text{free}} / \left\{\mathbf{u}^{(1)}\cdot\mathbf{n}\right\}_{\Gamma_\text{free}}$ is the effective curvature of the free surface.

Volume integrals in (12, 13) scale as $\langle\cdot\rangle_{\Omega_\text{n}} \sim h_n r_n^2$, and surface integrals scale as $\{\cdot\} \sim r_n^2$. In this study we consider cases in which the nozzle height is much shorter than the reference length, and expand the mass and energy conservation equations in terms of the small parameter $h_n \ll 1$. If $h_n L \simeq L$, however, then the terms proportional to h_n cannot be ignored and the flow should be modelled directly in the nozzle as well as in the channel. We approximate the flow velocity and the pressure by their values on the boundaries:

$$\mathbf{u}^{(1)} \simeq \mathbf{u}^{(1)}\Big|_{\Gamma_{\text{N}-\text{C}}} + \mathcal{O}\left(h_n\right), \quad P^{(1)} \simeq P^{(1)}\Big|_{\Gamma_\text{free}} + \mathcal{O}\left(h_n\right), \tag{14}$$

which gives $\left\langle\rho^{(1)}\right\rangle_{\Omega_\text{n}} = \left\langle P^{(1)}\right\rangle_{\Omega_\text{n}} \simeq \left|\Omega_\text{n}\right| P^{(1)}\big|_{\Gamma_\text{free}} + \mathcal{O}\left(h_n^2\right)$. Substituting that into (12) gives a mass balance approximation to second order in h_n:

$$\frac{d}{dt}\hat{\Omega}_\text{n} = -\epsilon\left\{\mathbf{u}^{(1)}\cdot\mathbf{n}\right\}_{\Gamma_{\text{N}-\text{C}}} - \epsilon\left|\Omega_\text{n}\right|\frac{d}{dt}\gamma\hat{\kappa} + \mathcal{O}\left(\epsilon^2, h_n^2\right). \tag{15}$$

The second term on the right hand side is proportional to h_n and accounts for the nozzle flow compressibility and potential energy.

Substituting (14) into (13) and using (11, 15) allows us to derive an energy-consistent approximation of the stress on the shared boundary $\Gamma_{\text{N}-\text{C}}$:

$$\sigma_{ij}^{(1)} n_j = -\gamma\hat{\kappa}n_i - h_n\left(\partial_t u_i^{(1)} - \frac{1}{Re}\Delta_\Gamma u_i^{(1)}\right) + \mathcal{O}\left(\epsilon^2, h_n^2\right) \quad \text{on } \Gamma_{\text{N}-\text{C}}. \tag{16}$$

Here Δ_Γ is the tangent Laplace operator on $\Gamma_{\mathrm{N-C}}$. The term on the right hand side proportional to h_n accounts for the internal and viscous effects in the fluid. The nozzle flow velocity on $\Gamma_{\mathrm{N-C}}$ is determined by the acoustic velocity on $\Gamma_{\mathrm{C-N}}$. Considering the inertial and viscous effects only in the static part of the nozzle domain h_{CL}, we obtain a nonlinear (through the curvature term $\hat{\kappa}$) acoustic impedance boundary condition:

$$\sigma_{ij} n_j = -\gamma \hat{\kappa} n_i - h_{\mathrm{CL}} \left(\partial_t u_i - \frac{1}{Re} \Delta_\Gamma u_i \right) \quad \text{on } \Gamma_{\mathrm{C-N}}. \tag{17}$$

2.2.2. Free surface parametrization

The above analysis is valid for fluid-gas interface of any shape. In this paper, inspired by experimental observations [39, 40, 41], we approximate the free surface as a spherical cap, $\Gamma_{\mathrm{free}} \simeq \hat{\Gamma}_{\mathrm{free}}$, neglecting the presence of large wavenumber capillary waves $k \gg \pi/R_n$ on Γ_{free}. This simplifies the analysis by providing a single parameter (curvature) to quantify the relationship betwen pressure and nozzle mass, but would need to be revised for non-spherical interfaces, which are observed at the end of the jetting process ([3], section 3). The approximate surface curvature is a uniform function and coincides with the effective surface curvature: $\gamma|_{\Gamma_{\mathrm{free}}} \simeq \gamma|_{\hat{\Gamma}_{\mathrm{free}}} = \hat{\kappa}(t)$. The approximated free surface is a hemisphere when $\hat{\kappa} = 1$. The surface area $\left|\hat{\Gamma}_{\mathrm{free}}(\hat{\kappa})\right|$ equals

$$\left|\hat{\Gamma}_{\mathrm{free}}(\hat{\kappa})\right| = \frac{r_n^2}{4} \frac{8\pi}{\hat{\kappa}^2} \left(1 - \cos\theta(\hat{\kappa})\right), \tag{18}$$

where $\cos\theta(\hat{\kappa}) \equiv \sqrt{1-\hat{\kappa}^2}$. The nondimensional energy of the free boundary with uniform curvature equals $\hat{E}_{\mathrm{free}} = \epsilon^{-1} \gamma \frac{r_n}{2} \left|\hat{\Gamma}_{\mathrm{free}}\right|$. The nozzle volume $|\Omega_{\mathrm{n}}|$ is a sum of the volume between the shared boundary $\Gamma_{\mathrm{N-C}}$ and the plane of the free surface contact line $\pi r_n^2 h_{\mathrm{CL}}$, and the volume enclosed between the plane of the free surface contact line and the free surface $\hat{\Omega}_{\mathrm{n}}$:

$$|\Omega_{\mathrm{n}}| = \pi r_n^2 h_{\mathrm{CL}} + \hat{\Omega}_{\mathrm{n}} = \pi r_n^2 h_{\mathrm{CL}} + \frac{r_n^3}{8} \frac{8\pi}{3} \frac{1}{\hat{\kappa}^3} \left(2 + \cos\theta(\hat{\kappa})\right) \left(1 - \cos\theta(\hat{\kappa})\right)^2. \tag{19}$$

The derivatives of the surface area and enclosed volume are functions of $\hat{\kappa}$:

$$\frac{8}{r_n^3} \frac{d\hat{\Omega}_{\mathrm{n}}(\hat{\kappa})}{d\hat{\kappa}} = \frac{4}{r_n^2} \frac{1}{\hat{\kappa}} \frac{d\left|\hat{\Gamma}_{\mathrm{free}}(\hat{\kappa})\right|}{d\hat{\kappa}} = \frac{8\pi}{\hat{\kappa}^4} \frac{\left(1 - \cos\theta(\hat{\kappa})\right)^2}{\cos\theta(\hat{\kappa})} \tag{20}$$

The contact line is static $\frac{d}{dt} h_{\mathrm{CL}} = 0$, and therefore $\frac{d}{dt} |\Omega_{\mathrm{n}}| = \frac{d}{dt} \hat{\Omega}_{\mathrm{n}}(\hat{\kappa}) = \frac{d\hat{\Omega}_{\mathrm{n}}(\hat{\kappa})}{d\hat{\kappa}} \frac{d}{dt} \hat{\kappa}$. The nozzle volume conservation equation (15) then becomes an ODE for the uniform curvature $\hat{\kappa}$:

$$\frac{d\hat{\Omega}_{\mathrm{n}}(\hat{\kappa})}{d\hat{\kappa}} \frac{d}{dt} \hat{\kappa} = -\epsilon \left\{ \mathbf{u}^{(1)} \cdot \mathbf{n} \right\}_{\Gamma_{\mathrm{N-C}}} - \epsilon h_{\mathrm{CL}} \left|\Gamma_{\mathrm{C-N}}\right| \frac{d}{dt} \gamma \hat{\kappa} \tag{21}$$

subject to an initial condition $\hat{\kappa}(t=0) = \hat{\kappa}_0$. Similarly to the stress boundary condition (17), the compressibility effects are accounted for only inside the static part of the nozzle domain.

The change of the nozzle system energy $\mathcal{E}_\mathrm{n}$ is consistent with the acoustic energy flux through $\Gamma_{\mathrm{C-N}}$:

$$\begin{aligned} \mathcal{E}_\mathrm{n} &= \epsilon^{-1}\gamma\frac{r_n}{2}\left|\hat{\Gamma}_\mathrm{free}\right| + \frac{1}{2}h_\mathrm{CL}\left(\left\{(\mathbf{u}\cdot\mathbf{n})^2\right\}_{\Gamma_{\mathrm{C-N}}} + |\Gamma_{\mathrm{C-N}}|\,(\gamma\hat{\kappa})^2\right), \\ \frac{d}{dt}\mathcal{E}_\mathrm{n} &= \mathcal{F}_{\mathrm{C-N}} = \{u_i, \sigma_{ij}n_j\}_{\Gamma_{\mathrm{C-N}}}. \end{aligned} \tag{22}$$

By combining the channel and the nozzle flows into one system, the total energy of the system changes due to the energy fluxes through the channel boundaries with prescribed velocity Γ_vel or force Γ_force, and the viscous and thermal dissipation $\mathcal{R}$:

$$\frac{d}{dt}\left(\mathcal{E}_\mathrm{ac} + \mathcal{E}_\mathrm{n}\right) = \{U_i, \sigma_{ij}n_j\}_{\Gamma_\mathrm{vel}} + \{u_i, f_i\}_{\Gamma_\mathrm{force}} - \mathcal{R}. \tag{23}$$

2.3. Direct problem discretization

We discretize the thermoviscous acoustic problem (4) in space using the finite elements package FEniCS [42]. We choose continuous Lagrange elements of order 2 for the velocity and temperature components, and of order 1 for the pressure component of $\mathcal{Q}_\mathrm{c}$ [43, 44], to construct the corresponding weak forms.

We divide the time domain $\mathcal{T}$ into N intervals of length Δt. Following [45], the mid-point rule $\theta = \frac{1}{2}$ is chosen to discretize the unsteady thermoviscous acoustic equation by a finite difference scheme. This choice of θ is equivalent to the non-dissipative, dispersive, second order accurate Crank–Nicolson scheme [46]. We choose a non-dissipative scheme because we want to minimize the error in the acoustic energy due to the numerical effects.

In order to reduce the cost of the unsteady computations, we choose such discretisation of the bilinear weak form that it is independent of time, and the matrix factorization could be stored and re-used each time step. This greatly reduces the computational time required to run a direct solver, and, as shown later, the adjoint solver backwards in time. Moreover, if one performs a direct-adjoint looping multiple times for optimization, the matrix still has to be factorized only once. The resulting linear system is solved with a direct solver MUMPS [47], for each time step.

3. Optimal control of coupled domains

3.1. Governing equations for the adjoint problems

Here we derive the adjoint counterpart of the coupled acoustic and nozzle flow system. The direct acoustic state $\mathcal{Q}_\mathrm{c}$ is defined in Σ_c and governed by the thermoviscous acoustic equations (4) and boundary conditions (5). The nozzle flow state $\mathcal{Q}_\mathrm{n}$ is characterized by the free surface

curvature ODE (21). The acoustic and nozzle flows are coupled via the boundary conditions (17) and the flow through the shared boundary. The acoustic energy and the flow energy inside the nozzle are defined by (6) and (22), respectively. We choose the total energy $\mathcal{E} = \mathcal{E}_{\text{ac}} + \mathcal{E}_{\text{n}}$ (23) at the final time t_f as the objective function $\mathcal{J}$:

$$\begin{aligned}\mathcal{J} &\equiv \mathcal{E}_{\text{ac}} + \mathcal{E}_{\text{n}} \\ &= \frac{1}{2}\left\langle \mathcal{Q}_{\text{c}}, \mathrm{A}_c \mathcal{Q}_{\text{c}} \right\rangle_{\Omega_{\text{c}}} + \gamma \frac{r_n}{2\epsilon}\left|\hat{\Gamma}_{\text{free}}\right| + \frac{h_{\text{CL}}}{2}\left(\left\{(\mathbf{u}\cdot\mathbf{n})^2\right\}_{\Gamma_{\text{C-N}}} + \left|\Gamma_{\text{C-N}}\right|(\gamma\hat{\kappa})^2\right) \quad \text{at } t = t_f.\end{aligned} \tag{24}$$

We multiply the acoustic state equations (4) by the adjoint acoustic variables $\Lambda_c^\dagger \equiv \left(\mathbf{u}^\dagger, P^\dagger, T^\dagger\right)$. We multiply the nozzle state equations (21) by $\epsilon^{-1}\gamma\kappa^\dagger$, where $\kappa^\dagger$ is the adjoint curvature variable. The augmented objective function is:

$$\begin{aligned}\mathcal{L} = \mathcal{J} &- \left[\Lambda_c^\dagger, \frac{\partial}{\partial t}\mathrm{A}_c\mathcal{Q}_{\text{c}} \ + \mathrm{B}_c\mathcal{Q}_{\text{c}}\right]_{\Sigma_{\text{c}}} \\ &- \left[\epsilon^{-1}\gamma\kappa^\dagger, \frac{d}{dt}\hat{\Omega}_{\text{n}} + \epsilon\left\{\mathbf{u}\cdot\mathbf{n}\right\}_{\Gamma_{\text{N-C}}} + \epsilon h_{\text{CL}}\left|\Gamma_{\text{C-N}}\right|\frac{d}{dt}\gamma\hat{\kappa}\right]_{\Sigma_{\text{n}}}.\end{aligned} \tag{25}$$

We set the variation of the Lagrangian $\delta\mathcal{L}$ with respect to the direct state to zero. After successive integration by parts and applying the initial and boundary conditions from (5), we obtain the adjoint acoustic equations,

$$-\frac{\partial}{\partial t}\mathrm{A}_c\Lambda_c^\dagger + \mathrm{B}_c^\dagger\Lambda_c^\dagger = 0 \quad \text{in} \quad \Sigma_{\text{c}}, \tag{26a}$$

$$\sigma_{ij}^\dagger n_j = -\gamma\kappa^\dagger n_i - h_{\text{CL}}\left(\partial_t + \frac{1}{Re}\Delta_\Gamma\right)u_i^\dagger \quad \text{on} \quad \Gamma_{\text{C-N}}, \tag{26b}$$

$$\Lambda_c^\dagger(\mathbf{x}, t = t_f) = \mathcal{Q}_{\text{c}}(\mathbf{x}, t = t_f), \tag{26c}$$

and the adjoint nozzle flow equations,

$$\left(\frac{d\hat{\Omega}_{\text{n}}}{d\hat{\kappa}}\right)\frac{d}{dt}\kappa^\dagger = \epsilon\left\{\mathbf{u}^\dagger\cdot\mathbf{n}\right\}_{\Gamma_{\text{N-C}}} - \epsilon\frac{d\left(\hat{\Omega}_{\text{n}}\hat{\kappa}\right)}{d\hat{\kappa}}\frac{d}{dt}\gamma\hat{\kappa} \quad \text{in} \quad \Sigma_{\text{n}}, \tag{27a}$$

$$\kappa^\dagger(t = t_f) = \hat{\kappa}(t = t_f). \tag{27b}$$

The adjoint acoustic operator $\mathrm{B}_c^\dagger$ is defined as

$$\mathrm{B}_c^\dagger = \begin{bmatrix} -\frac{1}{Re}\nabla_j\boldsymbol{\tau}_{ij} & -\nabla_i & 0 \\ -\nabla_i & 0 & 0 \\ 0 & 0 & -\frac{\Delta}{(\gamma_{th}-1)Pe} \end{bmatrix}. \tag{28}$$

The adjoint acoustic stress tensor is defined as $\sigma_{ij}^\dagger = -P^\dagger\delta_{ij} - Re^{-1}\tau_{ij}$. The adjoint no slip velocity and stress free boundary conditions, as well as the isothermal and adiabatic temperature

boundary conditions, are equal to the homogeneous boundary conditions of the direct problem [6].

In section 2.3, the direct channel and nozzle states were discretized in time using the Crank–Nicolson scheme. The adjoint state is approximated using the same method, resulting in a consistent time-discrete dual problem [48]. The symmetry between the direct and adjoint problems is discussed in Appendix A.

3.2. The augmented gradient

The top boundary of the channel contains a piezo-electric actuator, which we model as a prescribed velocity boundary condition $\mathcal{U}(t)$. We minimize the objective function $\mathcal{J}$ (24) by optimizing the velocity profile on the actuator boundary Γ_{act}. This control is described through a velocity Dirichlet boundary condition:

$$\mathbf{u} = \mathcal{U} \quad \text{on } \Gamma_{\mathrm{act}}.$$

The only non zero term in the Lagrangian variation (25) is the adjoint stress boundary integral on Γ_{act}. This equals the objective variation with respect to the control, and therefore the objective gradient is:

$$\mathcal{J}'[\delta\mathcal{U}] = \left\{\sigma^{\dagger}_{ij} n_j, \delta\mathcal{U}_i\right\}_{\Gamma_{\mathrm{act}}\times\mathcal{T}}. \tag{29}$$

In other words, the distribution of the adjoint stress along the control boundary is the sensitivity distribution.

4. Applications

4.1. One dimensional test case

In order to illustrate the method and to discuss the physical mechanisms it exploits, we first apply the optimization technique in section 3 to a one-dimensional test case. A viscous acoustic flow inside a unit length domain $\Omega_{\mathrm{c}} = \{x : 0 \le x \le 1\}$ is initially at rest $\mathcal{Q}_{\mathrm{c}}(x, t = 0) = 0$. The boundary at $x = 1$ is set as a control boundary. We prescribe a velocity profile $u(x = 1) = \mathcal{U}(t)$ on this boundary. The boundary at $x = 0$ is a free surface (21). This free surface is initially deformed $\hat{\kappa}(t = 0) = 0.05$, and therefore possesses non-zero initial energy $\mathcal{E}(t = 0) = \mathcal{E}_{\mathrm{n}}(t = 0) > 0$.

We define the nondimensional acoustic timescale t_{ac} to be the time taken for a wave to travel from $x = 0$ to $x = 1$. In these units the time taken for a wave to travel from one side to the other and back is $t_{\mathrm{L}} = 2$. This is a key quantity that will be referred to later. We discretize the

time domain $\mathcal{T}$ into equal intervals with time step $\Delta t = 10^{-4}$. The non-dimensional parameters of the experiment are provided in table 1. The optimization search space consists of control velocity values at each discrete time point $\mathcal{U}^n$ for $n = 1 \dots N-1$. The values of $\mathcal{U}^0, \mathcal{U}^N$ are fixed to zero. We use the `scipy.minimize(method='TNC')` [49] implementation of the truncated Newton method as the gradient-based algorithm to minimize the objective function (24). In all experiments, we use the Taylor remainder convergence test to ensure that the sensitivities calculated with the adjoint method are correct.

We start with the case in which the final time is set to $t_f = 2.5$ and use the gradient-based method to find the optimal waveform (figure 3a). Figure 3b shows the time history of the free surface energy $\mathcal{E}_{\mathrm{n}}$ (green line) and the acoustic energy $\mathcal{E}_{\mathrm{ac}}$ (blue line) in the optimally controlled case, normalized by the initial total energy value $\mathcal{E}(t = 0)$. The final energy at $\mathcal{E}(t = t_f)$ is 10^5 time lower than the initial value. In this simple case, the physical mechanism that it exploits can be clearly identified. The optimal waveform consist of three stages. The first stage is a pulse lasting $\tau_p = t_f - t_{\mathrm{L}} = 0.5$ that withdraws half the volume stored in the nozzle domain. In the second stage the actuator remains inactive while the front and back of the pulse reach the free surface at $t = 1$ and $t = 1 + \tau_p$ respectively. The pulse velocity amplitude doubles as it reflects from the free surface. The amount of fluid transferred through the free surface is therefore equal to the volume initially stored in the nozzle domain. At $t = 2$ the front of the reflected pulse reaches the actuator. Between these two times the free surface relaxes to zero curvature and, in doing so, reflects an acoustic pulse back towards the actuator. The third stage is a pulse lasting $\tau_p = t_f - t_{\mathrm{L}} = 0.5$ that withdraws more fluid such that the reflected pulse leaves the channel without further reflection and returns the fluid in the channel to its initial state at exactly $t = t_f$. The two pulses, when combined, withdraw exactly the mass of fluid between the initial and final positions of the surface.

For comparison we then examine the case in which the final time is set to $t_f = 3.0$ (figure 4). Figure 4b shows the time history of the free surface energy $\mathcal{E}_{\mathrm{n}}$ (green line) and the acoustic energy $\mathcal{E}_{\mathrm{ac}}$ (blue line) in the optimally controlled case, normalized by the initial total energy value $\mathcal{E}(t = 0)$. The optimal waveform is qualitatively identical to that found when $t_f = 2.5$ but with pulses lasting $\tau_p = t_f - t_{\mathrm{L}} = 1.0$ rather than $\tau_p = 0.5$. As before, the actuator withdraws exactly the half mass of fluid between the initial and final positions of the surface, but this time with a longer pulse and, consequently, with a smaller actuator velocity. Consideration of the physical mechanism shows that the optimization time has to be greater than $t_f = 2$ and that, beyond that, its lower limit will be determined by the maximum speed of the actuator. In both cases,

Table 1: Parameters of the optimization test case 4.1

	non-dimensional value
domain length, L	1
final time, t_f	2.5, 3
speed of sound, c_s	1
Mach number, ϵ	10^{-3}
Reynolds number, Re	$5 \cdot 10^3$
initial curvature, $\hat{\kappa}(t=0)$	0.05
surface tension, γ	0.01
nozzle radius, r_n	0.1
time step size, Δt	10^{-4}

the spurious oscillations in $\mathcal{U}$ appear due to step-like control at initial time (Gibbs phenomena).

4.2. Two dimensional straight channel

Having shown that the optimization algorithm works for a simple 1D case, and having identified the physical mechanism in that case, we now examine a 2D straight channel with a nozzle placed at the centre of one wall, an actuator along the opposite wall, an outlet boundary at the left side, and a symmetry boundary at the right side (figure 5). The dimensional parameters of the nozzle domain and acoustic constants are given in table 2. The spatial domain is discretized into $120 \cdot 10^3$ triangular elements [50]. In the remaining sections, we present the time and space scales in dimensional format because this enables easier comparison with the literature.

We assume that the nozzle state $\mathcal{Q}_{\mathrm{n}}$ shortly after the droplet has been expelled is a free surface with uniform curvature. For ease of demostration, we assume that the acoustic energy in the channel is zero. This assumption could easily be relaxed in practice. The simulation therefore starts from the zero acoustic state and non zero curvature:

$$\mathcal{Q}_{\mathrm{c}}(t=0) = 0, \quad \hat{\kappa}(t=0) = 0.25. \tag{30}$$

The objective is to minimize the total energy at the final time $\mathcal{J} = \mathcal{E}(t_f) = \mathcal{E}_{\mathrm{ac}}(t_f) + \mathcal{E}_{\mathrm{n}}(t_f)$ (24).

Typically the time between droplets is between 2 μs and 20 μs. In this paper, we calculate the open loop forcing that would need to be applied for periods of 1 μs, 2 μs and 3 μs in order to minimize the total energy at the end of the forcing period. We discretize the time domain

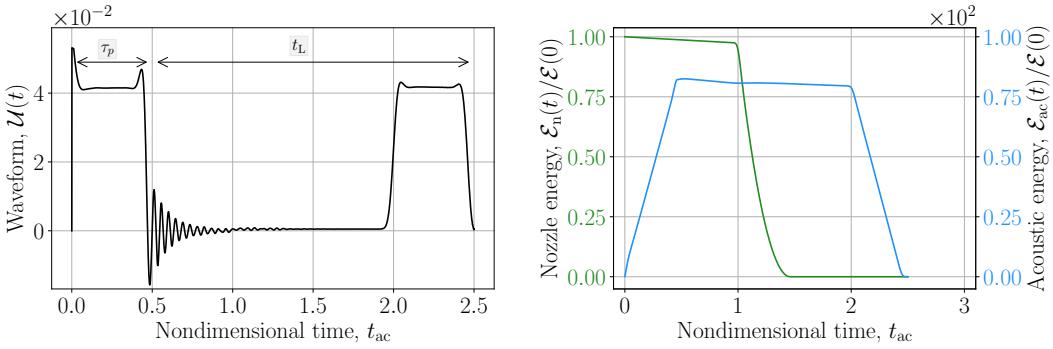

(a) (b)

Figure 3: Optimally controlled case of the one-dimensional unit length domain, $t_f = 2.5$. (a) the optimal velocity $\mathcal{U}$ of the control boundary, where τ_p indicates the pulse duration, and t_{L} is the timescale of the length of channel; (b) the nozzle energy (green), and acoustic energy (blue), normalized by the initial total energy value $\mathcal{E}(t = 0)$.

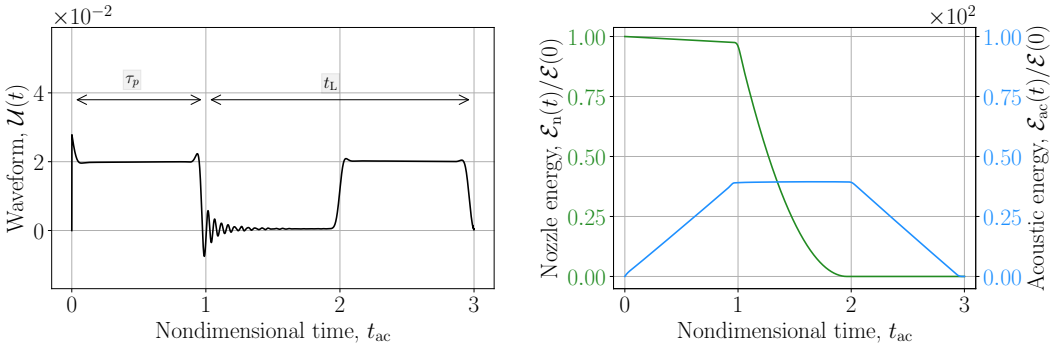

(a) (b)

Figure 4: Optimally controlled case of the one-dimensional unit-length domain, $t_f = 3$. (a) the optimal velocity $\mathcal{U}$ of the control boundary, where τ_p indicates the pulse duration, and t_{L} is the timescale of the length of channel; (b) the nozzle energy (green), and acoustic energy (blue), normalized by the initial total energy value $\mathcal{E}(t = 0)$.

Table 2: Inkjet microchannels parameters (section 4.2)

	dimensional value
final time, t_f, s	$(1-5)\cdot 10^{-6}$
speed of sound, c_s, m/s	10^3
Mach number, ϵ	10^{-3}
viscosity, μ, kg/(m · s)	$2\cdot 10^{-2}$
Prandtl number, Pr	10
initial curvature, $\kappa(t=0)$, m^{-1}	$0.05\cdot 10^6$
surface tension, γ, N/m	$50\ \cdot 10^{-3}$
nozzle radius, r_n, m	$10\ \cdot 10^{-6}$
nozzle length, l_n, m	$20\ \cdot 10^{-6}$
time step size, Δt, s	10^{-9}

$\mathcal{T}$ into equal time intervals with time step $\Delta t = 10^{-3}$ μs. This time step is chosen in order to have sufficient time resolution of the acoustic motion inside the narrowest part of the channel Ω_{c}, near the nozzle boundary.

The actuating waveforms in inkjet printing are constrained by the limitations of the driving electronics and response of the piezo-electric actuator. In this section, we assume that the piezo-electric actuator moves as a solid plate in the direction normal to the channel's wall. We model this as a boundary velocity $\mathcal{U}$ that is spatially uniform along the control boundary Γ_{act}. There is no mass flow through the actual physical actuator boundary, but we prescribe a velocity boundary condition on it. So there is effective mass flow through the fixed boundary used in computations. In 4.4, we compare the spatially uniform boundary control with a parabolic actuator velocity profile.

In practical devices the electric signal that forces the piezo-electric actuator is piecewise linear with a temporal resolution, w, between 0.01 μs and 0.1 μs. We use a continuous piecewise linear function in time to describe the boundary velocity.

In our model, shown in figure 5, the length of the control element (actuator boundary) varies from $L_{\mathrm{act}} = 20\mu$m to $L_{\mathrm{act}} = 200\mu$m. The waveform time resolution is fixed at $w = 0.1\mu$s. The left boundary is stress-free. The right boundary of the computational domain (shaded) is a symmetry plane. Figure 6 shows the optimized total energy at the final time $\mathcal{E}_{\mathrm{n}}(t_f)$ normalized by the uncontrolled total energy at the final time $\mathcal{E}^*(t_f)$. For 1μs optimization time there is

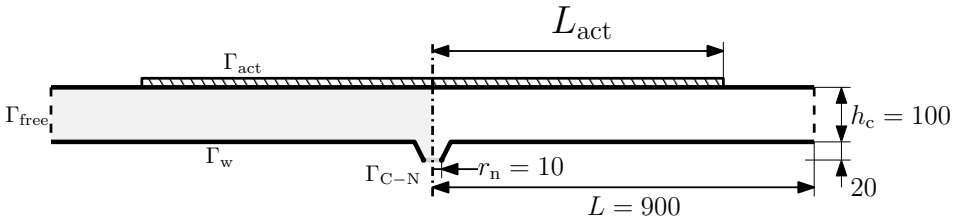

Figure 5: Two dimensional straight channel domain (sizes in μm).

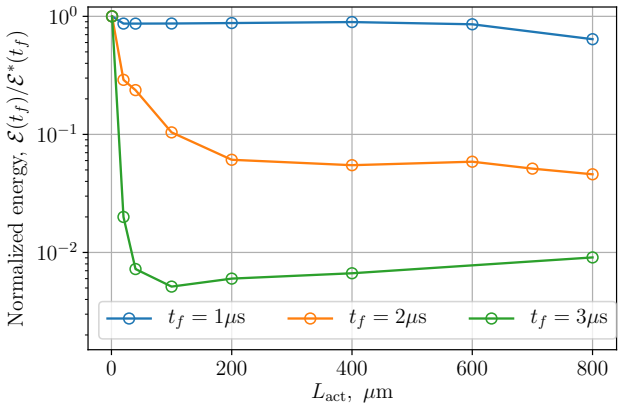

Figure 6: Optimized objective values for eight actuator lengths, L_{act}, and three final times, t_f. The values are normalized by the total energy at final time in the uncontrolled case.

almost no energy reduction because, as will be shown later, there is insufficient time to control the wave reflected by the left boundary. For 2μs optimization time the final energy reduces by one order of magnitude. For 3μs optimization time the final energy reduces by a further order of magnitude. The actuator size has little influence as long as it exceeds 100μm. The physical reasons for this are explored next.

4.2.1. Waveform optimization for $t_f = 2\mu s$.

For illustration, we will examine the results with final time $t_f = 2\mu$s and actuator length $L_{\text{act}} = 200\mu$m. Figure 7a shows the nozzle surface energy (green) and the total energy (blue) for the uncontrolled (dashed) and controlled (solid) cases. Figure 7b shows, for the uncontrolled case, the integrated acoustic energy dissipation (red dashed) and, for the controlled case, the total energy $\mathcal{E}(t)$ (blue), the integrated energy flux through the actuator boundary $\int \mathcal{F}_{\text{act}}(\tau)\mathrm{d}\tau$ (purple), the integrated acoustic energy dissipation $\int \mathcal{R}(\tau)\mathrm{d}\tau$ (red solid). Due to the energy balance (7), these are related by

$$\mathcal{E}(t) = \mathcal{E}(0) + \int_0^t \mathcal{F}_{\text{act}}(\tau)\mathrm{d}\tau - \int_0^t \mathcal{R}(\tau)\mathrm{d}\tau. \tag{31}$$

Figure 7c shows the mass flux through the actuator boundary (black) and the nozzle boundary (red). Figure 8 shows snapshots of the pressure field of the controlled case at times corresponding to the empty circles in figure 7a.

For the uncontrolled case, the nozzle surface energy $\mathcal{E}_{\text{n}}^*$ (green dashed line in figure 7a) reduces smoothly as the free surface relaxes. As for the one-dimensional test case, this sends an acoustic wave down the channel, increasing the acoustic energy. The total energy $\mathcal{E}^*$ (blue dashed line, figure 7a), which comprises the nozzle surface energy and the acoustic energy, reduces gently as the wave dissipates due to thermo-viscous mechanisms.

At time $t = t_f = 2.0$ μs, the controlled case has almost 20 times lower energy than the uncontrolled case (compare the solid blue and dashed blue lines in figure 7a). The optimal waveform (black line in figure 7c) consists of three phases. During the first phase $\mathcal{A}^+ : 0 \leq t \leq 0.38$ μs the actuator pulls fluid upwards and creates a negative pressure wave (figure 8a). This wave moves down towards the nozzle and left along the channel. The wave reaches the nozzle boundary at $t = 0.12\mu$s, at which point mass starts to be pulled out of the nozzle (red solid line in 7b), and the nozzle surface energy starts to reduce (green solid line in 7a). The wave reflects back off the nozzle, reaching the actuator at $t = 0.24\mu$s. Reverberations at this timescale, which is that of the height of the channel, continue during the controlled period. This behaviour is

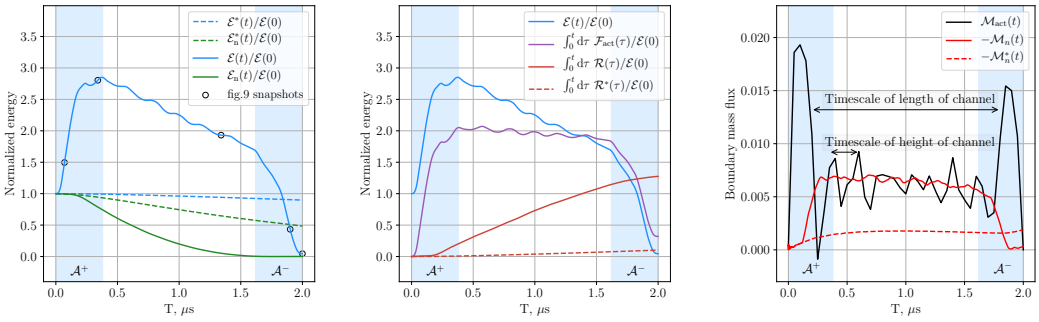

(a) (b) (c)

Figure 7: Comparison between the uncontrolled case (dashed lines) and the optimally controlled case (solid lines) with $L_{\text{act}} = 200\mu$m and $t_f = 2\mu$s. (a) Total energy $\mathcal{E}(t)$ (blue) and nozzle energy $\mathcal{E}_{\text{n}}(t)$ (green), normalized by $\mathcal{E}(t=0)$. (b) Integrated energy flux through the actuator boundary $\int \mathcal{F}_{\text{act}}(\tau)\text{d}\tau$ (purple line), integrated acoustic energy dissipation $\int \mathcal{R}(\tau)\text{d}\tau$ (red solid line), and the integrated acoustic energy dissipation $\int \mathcal{R}^*(\tau)\text{d}\tau$ in the uncontrolled case (red dashed line). (c) Boundary mass flux through the actuator boundary $\mathcal{M}_{\text{act}}$ (black) and the nozzle boundary $\mathcal{M}_{\text{n}}$ (red). The red dashed line is the mass flux $\mathcal{M}_{\text{n}}^*$ through the nozzle boundary in the uncontrolled case. The coloured patches denote the actuation phases, when the acoustic waves are formed ($\mathcal{A}^+$) and absorbed by the actuator ($\mathcal{A}^-$).

similar to that of the 1D test case but is more complicated because the flow is 2D. This wave relaxes the free surface but, unavoidably, produces a large amplitude wave moving left along the channel (figure 8b). Indeed the energy flux through the control boundary during the first phase, $\mathcal{A}^+$, is large and the total energy rapidly increases to nearly three times that of the uncontrolled case.

During the second phase $0.38 \leq t \leq 1.62$ μs the integrated mass flux through the actuator, $\mathcal{M}_{\text{act}} \equiv \{\mathbf{u}\cdot\mathbf{n}\}_{\Gamma_{\text{act}}}$, is almost identical to the integrated mass flux away from the nozzle, $\mathcal{M}_{\text{n}}$ (black and red solid lines in figure 7c). Compared with the first pulse, this motion is relatively slow, shown by the fact that the energy flux through the actuator boundary is small $\partial_t\mathcal{E} \simeq 0$. The nozzle surface energy reduces to nearly zero during this phase (green solid line in 7a). Meanwhile, in the channel, the pressure wave generated during the first phase reflects off the stress-free boundary and a positive pressure wave travels back towards the nozzle and the actuator (figure 8c). The total energy $\mathcal{E}$ steadily decreases due to viscous and thermal dissipation of the acoustic wave (figure 7b, red line).

The third phase $\mathcal{A}^-$: $1.62 \leq t \leq 2.0$ μs is the counterpart of the first phase $\mathcal{A}^+$. When the positive pressure wave reaches the symmetry plane of the channel the actuator quickly moves out of the domain again (black line in figure 7b) and optimally absorbs the acoustic energy (blue

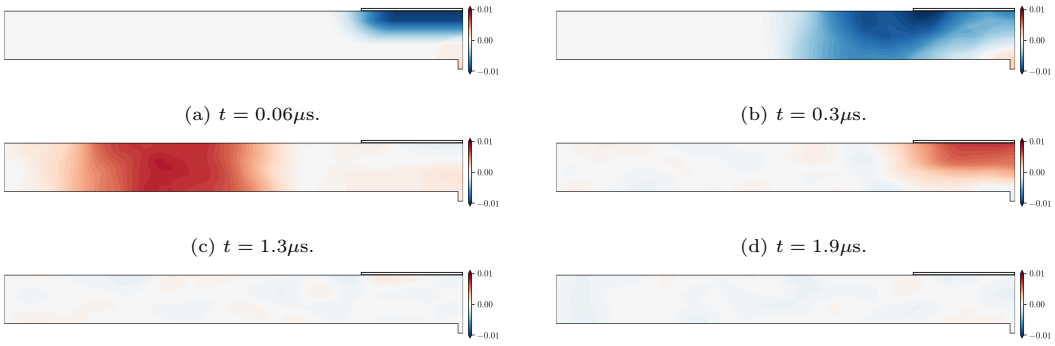

(a) $t = 0.06\mu$s. (b) $t = 0.3\mu$s.

(c) $t = 1.3\mu$s. (d) $t = 1.9\mu$s.

(e) $t = 2.0\mu$s. (f) $t = 2.5\mu$s.

Figure 8: Snapshots of the pressure distribution inside an injector channel at different times, with the optimal control applied to the actuator boundary, $L_{\text{act}} = 200\mu$m, $t_f = 2\mu$s. The actuator is the thin horizontal rectangle at the top-right of each frame.

line in figure 7b) by moving to make the wave do work on the actuator boundary (purple line in figure 7b). The acoustic pressure quickly reduces and remains small thereafter (fig. 8f). This acts on the timescale of the channel: $2L/c_s = 2 \times 900\mu\text{m}/\,(1000\text{m/s}) = 1.8\mu$s. If the optimization time is 1μs, the nozzle free surface energy could be reduced by the actuator but there would then be insufficient time to absorb the acoustic wave that is reflected off the stress-free boundary. The optimal solution is to do almost nothing.

We now investigate the effect of the actuator size L_{act} on the final energy and the optimal waveform. Figure 6 (orange line) shows the final total energy of the controlled cases, normalized by the final energy of the uncontrolled case. Figure 9 shows the optimal mass flux through the actuator boundary for different actuator sizes, L_{act}. All waveforms have the three-phase shape described above and exploit the same mechanism. The mass flux increases with the actuator length. This is because the actuators produce a wave that both pulls mass out of the nozzle and propagates to the stress free boundary, where it pulls mass through that boundary. The nozzle mass flux is determined by the mass in the nozzle and, with that mass flux fixed, the boundary mass flux then increases with the actuator length. Shorter actuators are therefore more efficient.

4.2.2. Waveform optimization for $t_f = 3\mu$s.

For illustration, we will examine the results with final time $t_f = 3\mu$s and actuator length $L_{\text{act}} = 100\mu$m. Figure 10 shows the time history of the energy and boundary mass fluxes for the uncontrolled and optimally controlled cases. Figure 11 shows snapshots of the pressure field at the times shown as open circles on figure 10.

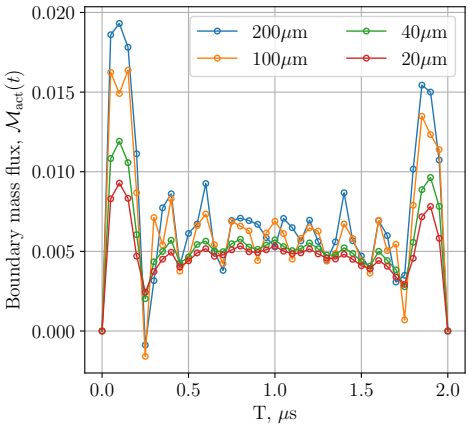

Figure 9: Optimal mass flux through the control boundary as a function of time, for different actuator lengths. The control duration is 2 μs.

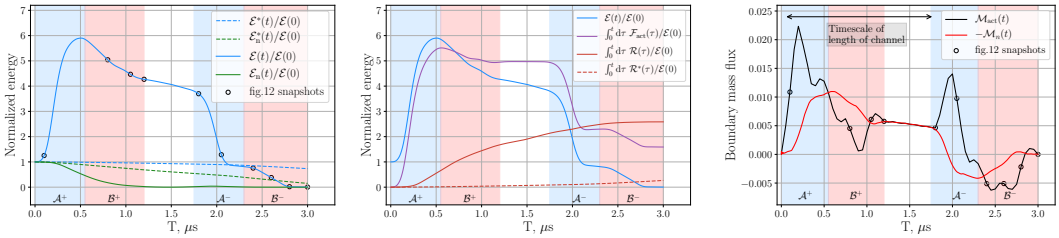

(a) (b) (c)

Figure 10: Comparison between the uncontrolled case (dashed lines) and the optimally controlled case (solid lines) with $L_{\rm act} = 100\mu$m and $t_f = 3\mu$s. (a) Total energy $\mathcal{E}(t)$ (blue) and nozzle energy $\mathcal{E}_{\rm n}(t)$ (green), normalized by $\mathcal{E}(t=0)$. (b) Integrated energy flux through the actuator boundary $\int \mathcal{F}_{\rm act}(\tau)\mathrm{d}\tau$ (purple line), integrated acoustic energy dissipation $\int \mathcal{R}(\tau)\mathrm{d}\tau$ (red solid line), and the integrated acoustic energy dissipation $\int \mathcal{R}^*(\tau)\mathrm{d}\tau$ in the uncontrolled case (red dashed line). (c) Boundary mass flux through the actuator boundary $\mathcal{M}_{\rm act}$ (black) and the nozzle boundary $\mathcal{M}_{\rm n}$ (red). The coloured patches denote the actuation phases, when the acoustic waves are formed ($\mathcal{A}^+, \mathcal{B}^+$) and absorbed by the actuator ($\mathcal{A}^-, \mathcal{B}^-$).

The first phase $\mathcal{A}^+ : 0 \leq t \leq 0.55$ μs is similar to the $\mathcal{A}^+$ phase of the $t_f = 2\mu$s case. The actuator pulls fluid upwards and generates a negative pressure wave (figure 11a). As before, the wave reaches the nozzle boundary at $t = 0.12\mu$s and mass starts to be pulled out of the nozzle. This wave reflects back off the nozzle. The reverberations in the fluid are as strong as in the previous case, but the actuator is wider. The wider actuator is unable to reduce the reverberations' amplitude without simultaneously creating high amplitude waves elsewhere. Therefore the actuator moves less in order to avoid creating these high amplitude waves elsewhere.

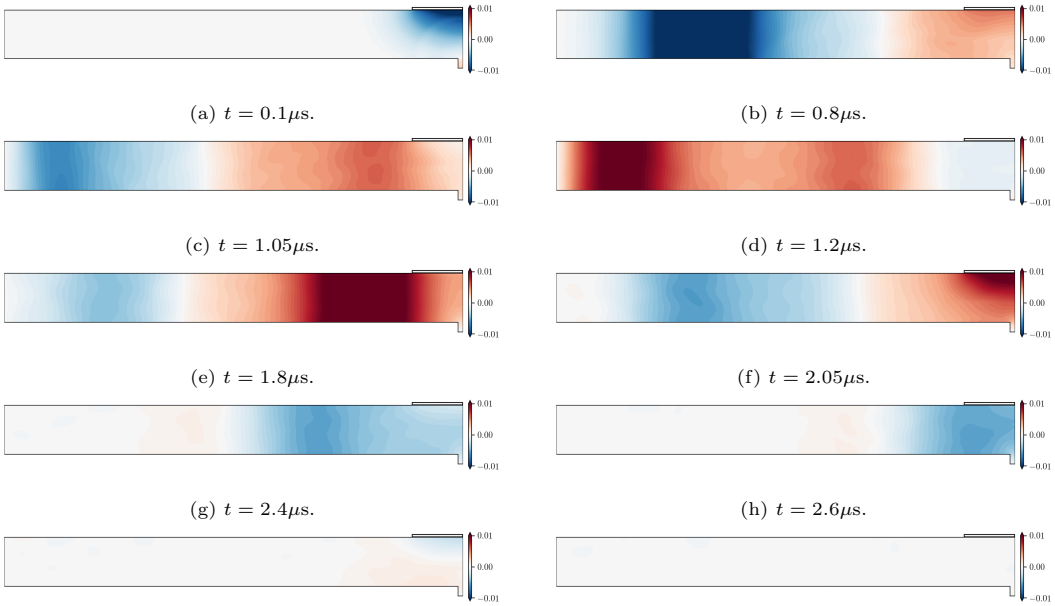

(a) $t = 0.1\mu$s. (b) $t = 0.8\mu$s.

(c) $t = 1.05\mu$s. (d) $t = 1.2\mu$s.

(e) $t = 1.8\mu$s. (f) $t = 2.05\mu$s.

(g) $t = 2.4\mu$s. (h) $t = 2.6\mu$s.

(i) $t = 2.8\mu$s. (j) $t = 3.0\mu$s.

Figure 11: Snapshots of the pressure distribution inside an injector channel at different times, with the optimal control applied to the actuator boundary, $L_{\text{act}} = 100\mu$m, $t_f = 3\mu$s. `channel_T_3_L_100.mp4` is a movie of the case (see supplementary materials).

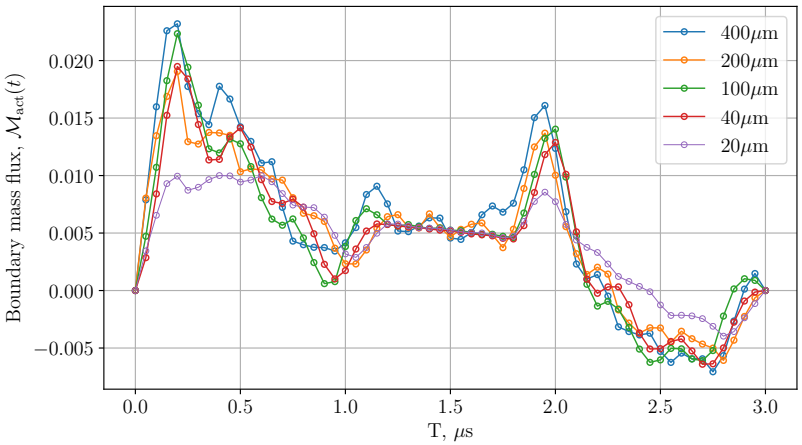

Figure 12: Optimal mass flux through the control boundary as a function of time, for different actuator lengths. The control duration is 3 μs.

As before, this motion produces a large amplitude wave moving left along the channel.

During the second phase $\mathcal{B}^+ : 0.55 \leq t \leq 1.2\mu$s the mass flux through the nozzle reaches a maximum. The actuator is still moving upwards, partially compensating for the flow from the nozzle and slowly absorbing the acoustic energy. A positive pressure wave moves left along the channel (fig. 11b). (The optimization algorithm does not create this wave for the 2μs case because there is insufficient time to cancel it.) During this phase, almost all of the fluid is quickly transferred from the nozzle to the channel. By the end of the $\mathcal{B}^+$ phase, the free surface has nearly reached its final low energy state.

During the third phase $1.2 \leq t \leq 1.75\mu$s the mass flux from the actuator broadly cancels that from the nozzle. No new pressure waves form during this phase (fig.11c). The negative pressure left-running wave reflects from the open end (11d) and becomes a positive pressure right-running wave. This middle phase is similar to the middle phase of the $t_f = 2\mu$s case.

The fourth phase $\mathcal{A}^- : 1.8 \leq t \leq 2.3\mu$s is the same as the $\mathcal{A}^-$ phase in the $t_f = 2\mu$s case. The positive right-running wave is absorbed by the actuator (fig. 11e, 11f). This results in a rapid decrease in total energy. Meanwhile the positive left-running wave has reflected from the open end and has become a negative right-running wave. During the fifth phase $\mathcal{B}^- : 2.3 \leq t \leq 3.0\mu$s, the negative left-running pressure wave reaches the actuator, and is optimally absorbed by doing work on the actuator boundary. Figure 12 shows the mass flow at the actuator $\mathcal{M}_{\text{act}}$ as a function of time for different L_{act}. The shapes of the waveforms for $t_f = 3\mu$s with different actuator lengths are similar. The increase of mass flux with actuator length is less pronounced

because the combination of $\mathcal{A}^+$, $\mathcal{B}^+$ waves pulls less fluid through the stress-free boundary than the $\mathcal{A}^+$ wave alone.

In summary, the most effective control to minimize the energy at the final time is achieved when the actuator moves out of the domain and provides a negative pressure pulse to accelerate the flow at the nozzle, and then adapts to the large mass flux during the $\mathcal{B}^+$ phase. This combination efficiently transfers all fluid from the nozzle to the channel and leaves sufficient time for the actuator to absorb the reflected waves afterwards. At lower optimization times, reasonably effective control can be achieved with a short negative pulse, followed by a long middle period in which the channel slowly absorbs the fluid from the nozzle, leaving sufficient time to cancel its reverberation from the ends of the channel. If there is insufficient time to cancel the reverberation from the ends of the channel then any control is ineffective. This shows that the minimum optimization time (i.e. the minimum time between droplet ejections) is $2L/c_s$.

4.3. Two dimensional U-shaped print head channel

Having shown that the optimization algorithm works for a straight channel, and having highlighted the importance of wave reflections at the ends of the channel, we now examine a realistic case, in which the ends of the channel bend upwards to make a U-shape and the length along the centreline is $L = 1235\mu$m (figure 13). We set the actuator length to $L_{\text{act}} = 400\mu$m. The spatial domain is discretized into $245 \cdot 10^3$ triangular elements [50].

From the snapshots (figure 15) we see that the waves disperse slightly as they travel round the corner. By comparing figure 14 with figure 10, however, we see that the optimal profiles for the U-shaped channel are qualitatively identical to those for the long straight channel in section 4.2.2. From this, and the snapshots, we deduce that the optimization method is exploiting the same physical mechanism.

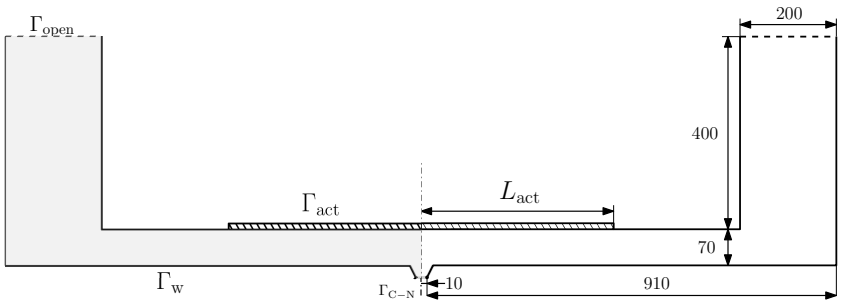

Figure 13: Printhead microchannel domain (sizes in μm). The right boundary is a symmetry plane.

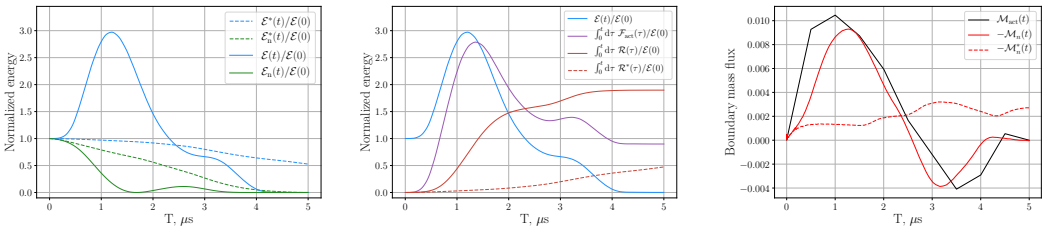

(a) (b) (c)

Figure 14: Comparison between the printhead uncontrolled case (dashed lines) and the optimally controlled case (solid lines) with $L_{\text{act}} = 400\mu$m and $t_f = 5\mu$s. (a) Total energy $\mathcal{E}(t)$ (blue) and nozzle energy $\mathcal{E}_{\text{n}}(t)$ (green), normalized by $\mathcal{E}(t = 0)$. (b) Integrated energy flux through the actuator boundary $\int_0^t \mathcal{F}_{\text{act}}(\tau)\text{d}\tau$ (purple line), integrated acoustic energy dissipation $\int \mathcal{R}(\tau)\text{d}\tau$ (red solid line), and the integrated acoustic energy dissipation $\int \mathcal{R}^*(\tau)\text{d}\tau$ in the uncontrolled case (red dashed line). (c) Boundary mass flux through the actuator boundary $\mathcal{M}_{\text{act}}$ (black) and the nozzle boundary $\mathcal{M}_{\text{n}}$ (red). The red dashed line is the mass flux $\mathcal{M}_{\text{n}}^*$ through the nozzle boundary in the uncontrolled case.

Finally we investigate how the objective value changes when we increase the waveform time resolution from $w = 1.0$ to $w = 0.5$, and 0.25μs. These correspond to the time resolution of state-of-the-art piezoelectric controllers. We project the optimal waveform with $w = 1.0\mu$s (figure 16b, solid line) to a higher dimensional space with $w = 0.5\mu$s, and use the projected solution as the initial guess for a new optimization problem. The optimal waveform for $w = 0.5\mu$s (figure 16b, dash-dotted line) results in 25% lower objective value (figure 16a). The optimal waveform for $w = 0.25\mu$s (figure 16b, dotted line) results in further 4% reduction in the objective value. These improvements are quite small, showing that the rather basic sinusoid-type waveform for the $w = 1.0\mu$s case provides a good trade-off between efficiency and complexity. This waveform is an outward moving pulse lasting 2.7μs, and an inwards moving pulse lasting 2 μs. The outward pulse causes the free surface to relax but generates acoustic waves that travel down the channel. These reflect and first arrive back at the actuator at $t = 2.4\mu$s. The trailing edge of the outward pulse and then the inward pulse absorb these reflected waves optimally. Given that this waveform would be imposed just after ejection of the droplet, it is reassuringly similar to the W-shaped waveform that, by trial and error, has been shown to remove residual acoustic waves arising from the previous ejection cycle [24]. The total energy reduces to nearly zero, so if there is another local minimum, it cannot be significantly better than this one. The advance in this paper is to show this rigorously with adjoint-based optimization in the time domain, to identify the physical mechanisms that this waveform exploits, and to employ a general method that can be applied to other geometries.

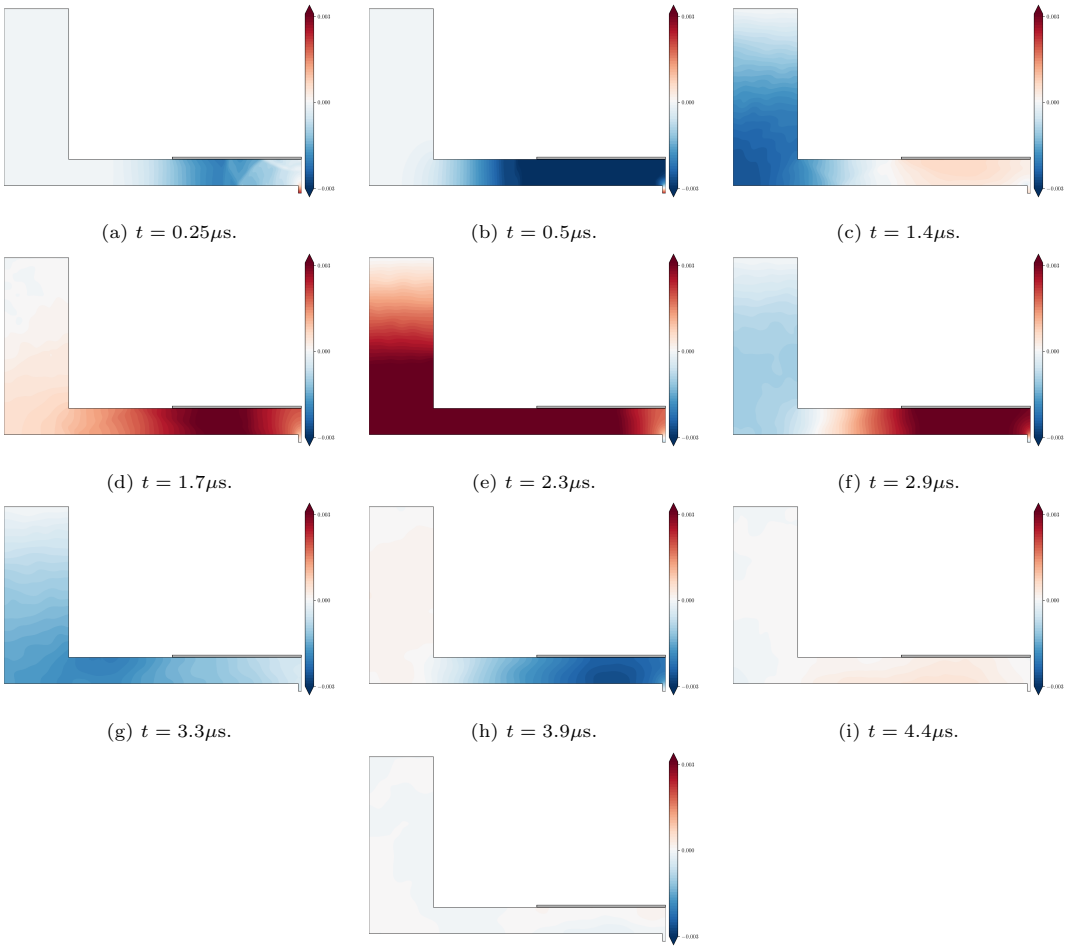

(a) $t = 0.25\mu$s. (b) $t = 0.5\mu$s. (c) $t = 1.4\mu$s.

(d) $t = 1.7\mu$s. (e) $t = 2.3\mu$s. (f) $t = 2.9\mu$s.

(g) $t = 3.3\mu$s. (h) $t = 3.9\mu$s. (i) $t = 4.4\mu$s.

(j) $t = 5.0\mu$s.

Figure 15: Snapshots of the pressure distribution inside a U-shaped printhead at different times, with the optimal control applied to the actuator boundary, $L_{\text{act}} = 400\mu$m, $t_f = 5\mu$s. `printhead_T_5_L_400.mp4` is a movie of the case (see supplementary materials).

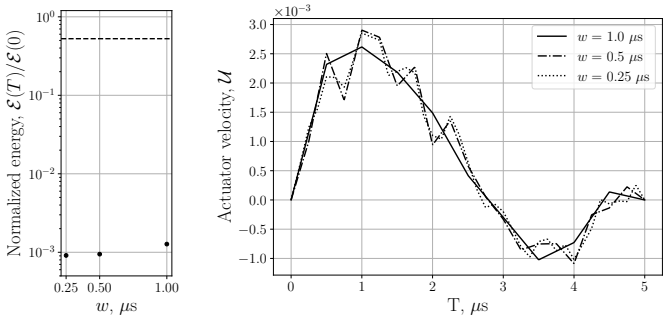

(a) (b)

Figure 16: (a) Optimized objective values (total energy at the final time $\mathcal{E}(T)$ normalized by initial value $\mathcal{E}(0)$) for different waveform resolution w, and (b) corresponding waveforms.

4.4. Optimization with a parabolic actuator velocity profile

In previous sections, the flow inside a straight and a U-shaped channels driven by an actuator with a uniform actuator velocity profile has been optimized. This section examines a system with a parabolic actuator velocity profile, and two cases are considered: a straight channel with $L_{\text{act}} = 200\mu$m, $t_f = 2\mu$s (similar to 4.2), and a U-shaped channel with $L_{\text{act}} = 400\mu$m, $t_f = 5\mu$s (similar to 4.3). The velocity boundary condition on Γ_{act} is $\mathbf{u} = c(t)\,(x - x_{\text{act}})\,(x - x_{\text{act}} - 2L_{\text{act}})\,\mathbf{n}$, where x is the coordinate along the actuator boundary, and x_{act} is the position of the leftmost point on the actuator boundary.

The same optimization strategy as descried in section 4.1 is applied to find an optimal waveform. Figure 17 shows an optimal waveform, and a mass and energy fluxes for a straight channel (figure 5) and $t_f = 2\mu$s (dashed lines). Solid lines denote the optimized results for a flat actuator velocity profile (from section 4.2). The optimal waveforms (figure 17c) for parabolic and flat velocity profiles are very similar, and the energy transfer between the nozzle, channel, and the actuator follow the same pattern (figure 17b).

Figure 18 shows optimization results for a U-shaped printhead channel (the same as in section 4.3) with a parabolic actuator velocity profile. Again, the parabolic profile results (dashed lines) match very closely the optimization results for a uniform profile (solid lines). This means that the energy damping mechanism is independent of the exact shape of the actuator velocity profile, and is governed by the mass flow through the actuator boundary $\mathcal{M}_{\text{act}}$.

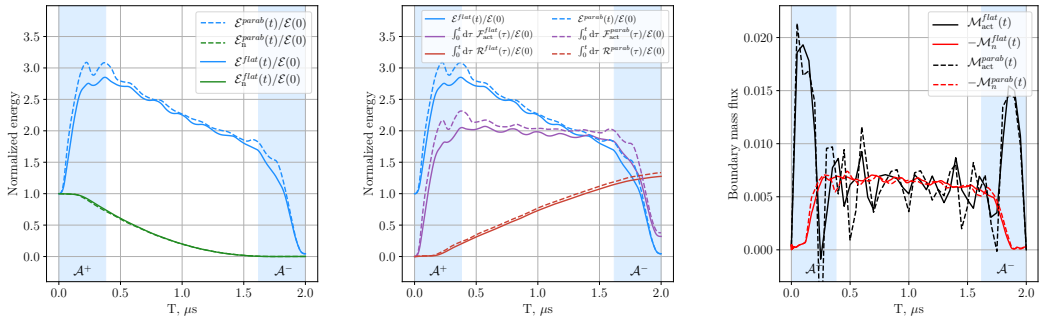

(a) (b) (c)

Figure 17: Comparison between the optimally controlled straight channel flow with flat (solid lines) and parabolic (dahsed lines) actuator velocity profiles with $L_{\text{act}} = 200\mu$m and $t_f = 2\mu$s. (a) Total energy $\mathcal{E}_{\text{n}}(t)$ (blue) and nozzle energy $\mathcal{E}_{\text{n}}(t)$ (green), normalized by $\mathcal{E}(t=0)$. (b) Integrated energy fluxes through the actuator boundary $\int \mathcal{F}_{\text{act}}(\tau)\text{d}\tau$ (purple line), integrated acoustic energy dissipation $\int \mathcal{R}(\tau)\text{d}\tau$ (red solid line). (c) Boundary mass fluxes through the actuator boundary $\mathcal{M}_{\text{act}}$ (black) and the nozzle boundary $\mathcal{M}_{\text{n}}$ (red). The coloured patches denote the actuation phases, when the acoustic waves are formed ($\mathcal{A}^+$) and absorbed by the actuator ($\mathcal{A}^-$).

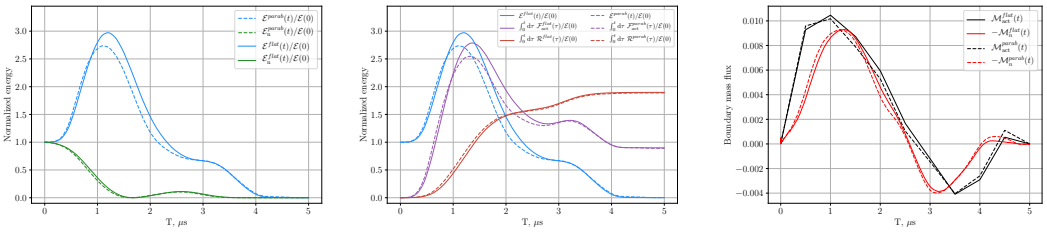

(a) (b) (c)

Figure 18: Comparison between the optimally controlled printhead flow with flat (solid lines) and parabolic (dahsed lines) actuator velocity profiles with $L_{\text{act}} = 400\mu$m and $t_f = 5\mu$s. (a) Total energy $\mathcal{E}(t)$ (blue) and nozzle energy $\mathcal{E}_{\text{n}}(t)$ (green), normalized by $\mathcal{E}(t=0)$. (b) Integrated energy fluxes through the actuator boundary $\int_0^t \mathcal{F}_{\text{act}}(\tau)\text{d}\tau$ (purple line), integrated acoustic energy dissipation $\int \mathcal{R}(\tau)\text{d}\tau$ (red solid line). (c) Boundary mass fluxes through the actuator boundary $\mathcal{M}_{\text{act}}$ (black) and the nozzle boundary $\mathcal{M}_{\text{n}}$ (red).

5. Conclusions

In this paper we develop a gradient-based approach that uses adjoint methods in the time domain to optimize the deformation of the piezo-electric actuator in an inkjet microchannel. We show that an optimally controlled actuator can reduce the total energy inside the printhead microchannel geometry by 1000 times, compared with the uncontrolled case. The actuator's initial movement withdraws fluid from the nozzle. The liquid/gas surface relaxes towards the zero curvature state. This initial movement sends an acoustic wave down the microchannel,

which reflects off the open end and returns some time later. The actuator then moves in order to perfectly absorb the reflected acoustic wave. The minimum time over which optimization can be successful, which is therefore the minimum time between droplets, is the time taken for an acoustic wave to travel from the actuator to the open end and back. The duration of the waveform itself must be added to this time. Short waveforms (e.g. $\mathcal{A}^+$ in figure 7c) are in one direction only and reduce the energy by just over one order of magnitude. Longer optimization times allow sufficient time for the waveform to have two components in opposite directions (e.g. $\mathcal{A}^+$ and $\mathcal{B}^+$ in figure 10c). This waveform reduces the free surface energy more quickly and by over a further order of magnitude.

This paper demonstrates the success of a more systematic approach than that currently used in industry: adjoint-based optimization of the waveform using numerical simulations, which can be interpreted physically. At a minimum, this physical understanding is useful in narrowing down the range of waveforms tested experimentally by trial and error. At best, this technique shows how to use numerical simulations in order to systematically and efficiently find the optimal waveform and the minimum time between drops in inkjet print heads.

This method can easily be applied to microchannels with complex geometry in three dimensions. The same method can be used to perform waveform optimization for the droplet ejection, in order to control the droplet volume and momentum. This would require a new nozzle model and a new objective function, but the channel model and optimization method would remain the same. Validation of the formulation and the numerical solution is the subject of future work.

Acknowledgements

This project has received funding from the European Union's Horizon 2020 research and innovation programme under the Marie Sklodowska-Curie grant agreement No 675008.

(Supplementary Material)

`channel_T_2_L_200.mp4` is a movie of the case in figures 7 and 8.

`channel_T_3_L_100.mp4` is a movie of the case in figures 10 and 11.

`printhead_T_5_L_400.mp4` is a movie of the case in figures 14 and 15.

Appendix A. The primal–adjoint problems symmetry

The symmetry between the direct (4, 21) and the adjoint problems (26, 27) has been discussed in [6]. In the frequency domain, performing complex conjugation and then inverting the sign of the velocity component makes the adjoint problem equivalent to the direct problem. Complex conjugation in the frequency domain translates to time inversion in the time domain: $t \to -t$. The velocity sign change has the same effect. We introduce a symmetry operator, $\mathbb{S} : \Lambda_c^\dagger \to \check{\Lambda}_c^\dagger = \left(-\mathbf{u}^\dagger, P^\dagger, T^\dagger\right)(-t) \equiv \left(\check{\mathbf{u}}^\dagger, \check{P}^\dagger, \check{T}^\dagger\right)(\check{t})$. We apply the symmetry operator to the coupled adjoint problems (26, 27), which results in

$$\frac{\partial}{\partial \check{t}} \mathrm{A}_c \check{\Lambda}_c^\dagger + \mathrm{B}_c^\dagger \check{\Lambda}_c^\dagger = 0 \quad \text{in} \quad \check{\Sigma}_c, \tag{A.1a}$$

$$\check{\sigma}_{ij}^\dagger n_j = -\gamma \kappa^\dagger n_i - h_{\mathrm{CL}} \left(\check{\partial}_t - \frac{1}{Re} \Delta_\Gamma \right) \check{u}_i^\dagger \quad \text{on} \quad \Gamma_{\mathrm{C-N}}, \tag{A.1b}$$

$$\mathbb{S}^{-1} \check{\Lambda}_c^\dagger(\mathbf{x}, t = t_f) = \mathcal{Q}_{\mathrm{c}}(\mathbf{x}, t = t_f), \tag{A.1c}$$

and

$$\left(\frac{d\hat{\Omega}_{\mathrm{n}}}{d\hat{\kappa}} \right) \frac{d}{d\check{t}} \kappa^\dagger = -\epsilon \left\{ \check{\mathbf{u}}^\dagger \cdot \mathbf{n} \right\}_{\Gamma_{\mathrm{N-C}}} - \epsilon \frac{d\left(\hat{\Omega}_{\mathrm{n}} \hat{\kappa}\right)}{d\hat{\kappa}} \frac{d}{d\check{t}} \gamma \hat{\kappa} \quad \text{in} \quad \check{\Sigma}_n, \tag{A.2a}$$

$$\kappa^\dagger(t = t_f) = \hat{\kappa}(t = t_f). \tag{A.2b}$$

After applying the symmetry operator, $\mathbb{S}$, to the adjoint problem, the temporal components of Σ_{c} and Σ_{n} change such that the adjoint flow propagates forward in time, in $\check{\mathcal{T}} = -\mathcal{T}$. The updated adjoint stress tensor is $\check{\sigma}_{ij}^\dagger = -\check{P}^\dagger \delta_{ij} + Re^{-1} \check{\tau}_{ij}^\dagger$. The initial condition for $\check{\Lambda}_c^\dagger$ (A.2b) implies that time integration of the adjoint problem should start from the direct state $\mathcal{Q}_{\mathrm{c}}(\mathbf{x}, t = t_f)$, but with the velocity vector pointing in the opposite direction. The adjoint system now has the same form as the direct systems (4, 21), with the difference that the terms $d\hat{\Omega}_{\mathrm{n}}/d\hat{\kappa}, d\left(\hat{\Omega}_{\mathrm{n}}\hat{\kappa}\right)/d\hat{\kappa}$ in (A.2a) come from the solution of the direct problem: the adjoint curvature follows the trajectory defined by the direct curvature $\hat{\kappa}$.

We perform the spatial discretization of the transformed adjoint problem in the same way as that of the direct problem in section 2.3. By applying the symmetry operator, the bilinear forms of the discrete direct and adjoint problem coincide, while the linear forms naturally differ.

References

[1] H. Tijdeman, On the propagation of sound waves in cylindrical tubes, Journal of Sound and Vibration 39 (1975) 1–33.

[2] W. Beltman, Viscothermal wave propagation including acousto-elastic interaction, part i: theory, Journal of Sound and Vibration 227 (1999) 555–586.

[3] D. Lohse, Fundamental fluid dynamics challenges in inkjet printing, Annual Review of Fluid Mechanics 54 (2022) 349–382.

[4] O. A. Basaran, H. Gao, P. P. Bhat, Nonstandard inkjets, Annual Review of Fluid Mechanics 45 (2013) 85–113.

[5] H. Li, J. Liu, K. Li, Y. Liu, Piezoelectric micro-jet devices: A review, Sensors and Actuators A: Physical (2019) 111552.

[6] P. V. Kungurtsev, M. P. Juniper, Adjoint-based shape optimization of the microchannels in an inkjet printhead, Journal of Fluid Mechanics 871 (2019) 113—138.

[7] D. B. Bogy, F. E. Talke, Experimental and theoretical study of wave propagation phenomena in drop-on-demand ink jet devices, IBM Journal of Research and Development 28 (1984) 314–321.

[8] J. Dijksman, Hydrodynamics of small tubular pumps, Journal of Fluid Mechanics 139 (1984) 173–191.

[9] W. Beltman, Viscothermal wave propagation including acousto-elastic interaction, part ii: Applications, Journal of Sound and Vibration 227 (1999) 587–609.

[10] M.-w. He, L.-l. Sun, K.-y. Hu, Y.-l. Zhu, H.-n. Chen, Analysis of dod inkjet printhead performance for printable electronics fabrication using dynamic lumped element modeling and swarm intelligence based optimal prediction, Journal of Central South University 22 (2015) 3925–3934.

[11] M. Berggren, A. Bernland, D. Noreland, Acoustic boundary layers as boundary conditions, Journal of Computational Physics 371 (2018) 633–650.

[12] A. U. Chen, O. A. Basaran, A new method for significantly reducing drop radius without reducing nozzle radius in drop-on-demand drop production, Physics of fluids 14 (2002) L1–L4.

[13] H.-C. Wu, H.-J. Lin, Y.-C. Kuo, W.-S. Hwang, Simulation of droplet ejection for a piezoelectric inkjet printing device, Materials Transactions 45 (2004) 893–899.

[14] I. Fumagalli, N. Parolini, M. Verani, Optimal control in ink-jet printing via instantaneous control, Computers & Fluids 172 (2018) 264–273.

[15] J. C. Miers, W. Zhou, Droplet formation at megahertz frequency, AIChE Journal 63 (2017) 2367–2377.

[16] R. L. Adams, J. Roy, A one-dimensional numerical model of a drop-on-demand ink jet, Journal of Applied Mechanics 53 (1986) 193–197.

[17] J. Eggers, T. F. Dupont, Drop formation in a one-dimensional approximation of the navier–stokes equation, Journal of fluid mechanics 262 (1994) 205–221.

[18] H. Jiang, H. Tan, One dimensional model for droplet ejection process in inkjet devices, Fluids 3 (2018) 28.

[19] D. Bogy, Drop formation in a circular liquid jet, Annual Review of Fluid Mechanics 11 (1979) 207–228.

[20] C. Galusinski, P. Vigneaux, On stability condition for bifluid flows with surface tension: Application to microfluidics, Journal of Computational Physics 227 (2008) 6140–6164.

[21] S. Manservisi, R. Scardovelli, A variational approach to the contact angle dynamics of spreading droplets, Computers & fluids 38 (2009) 406–424.

[22] C. Cossu, An introduction to optimal controllecture notes from the flow-nordita summer school on advanced instability methods for complex flows, Applied Mechanics Reviews 66 (2014).

[23] N. Pollini, O. Lavan, O. Amir, Adjoint sensitivity analysis and optimization of hysteretic dynamic systems with nonlinear viscous dampers, Structural and Multidisciplinary Optimization 57 (2018) 2273–2289.

[24] H. Gan, X. Shan, T. Eriksson, B. Lok, Y. Lam, Reduction of droplet volume by controlling actuating waveforms in inkjet printing for micro-pattern formation, Journal of micromechanics and microengineering 19 (2009) 055010.

[25] A. A. Khalate, X. Bombois, R. Babuška, H. Wijshoff, R. Waarsing, Performance improvement of a drop-on-demand inkjet printhead using an optimization-based feedforward control method, Control Engineering Practice 19 (2011) 771–781.

[26] A. A. Khalate, X. Bombois, S. Ye, R. Babuška, S. Koekebakker, Minimization of cross-talk in a piezo inkjet printhead based on system identification and feedforward control, Journal of Micromechanics and Microengineering 22 (2012) 115035.

[27] K.-S. Kwon, Waveform design methods for piezo inkjet dispensers based on measured meniscus motion, Journal of Microelectromechanical Systems 18 (2009) 1118–1125.

[28] B. Snyder, M. Yang, S. Singhal, O. Abed, S. Sreenivasan, Automated tuning of high-order waveforms for picoliter resolution jetting of rheologically challenging materials, Precision Engineering 56 (2019) 143–155.

[29] P. Luchini, A. Bottaro, Adjoint equations in stability analysis, Annual Review of fluid mechanics 46 (2014).

[30] S. Nadarajah, A. Jameson, A comparison of the continuous and discrete adjoint approach to automatic aerodynamic optimization, in: 38th Aerospace Sciences Meeting and Exhibit, 2000, p. 667.

[31] M. P. Juniper, Triggering in the horizontal rijke tube: non-normality, transient growth and bypass transition, Journal of Fluid Mechanics 667 (2011) 272.

[32] J. Brewster, M. P. Juniper, Shape sensitivity of eigenvalues in hydrodynamic stability, with physical interpretation for the flow around a cylinder, European Journal of Mechanics-B/Fluids 80 (2020) 80–91.

[33] J. C. Miers, W. Zhou, Droplet formation at megahertz frequency, AIChE Journal 63 (2017) 2367–2377.

[34] F. Culick, M. V. Heitor, J. H. Whitelaw, Unsteady combustion, volume 306, Springer Science & Business Media, 2012.

[35] G. S. Kell, Isothermal compressibility of liquid water at 1 atm., Journal of Chemical and Engineering Data 15 (1970) 119–122.

[36] B.-T. Chu, On the energy transfer to small disturbances in fluid flow (part i), Acta Mechanica 1 (1965) 215–234.

[37] L. Rayleigh, On the capillary phenomena of jets, Proc. R. Soc. London 29 (1879) 71–97.

[38] S. Popinet, Numerical models of surface tension, Annual Review of Fluid Mechanics 50 (2018) 49–75.

[39] W.-K. Hsiao, S. D. Hoath, G. D. Martin, I. M. Hutchings, Jetting, in-nozzle meniscus motion and nozzle-plate flooding in an industrial drop-on-demand print head, in: NIP & Digital Fabrication Conference, 1, Society for Imaging Science and Technology, 2011, pp. 66–69.

[40] J. Yang, H. Kim, B. Cho, J. Chung, Modeling of sessile droplet oscillation on electrohydrodynamic jetting nozzle at constant back pressure, Journal of Mechanical Science and Technology 28 (2014) 2815–2823.

[41] M.-J. van der Meulen, H. Reinten, F. Dijksman, D. Lohse, M. Versluis, Experimental techniques for retrieving flow information from within inkjet nozzles, Journal of imaging science and technology 60 (2016) 40502–1.

[42] A. Logg, K.-A. Mardal, G. N. Wells, et al., Automated Solution of Differential Equations by the Finite Element Method, Springer, 2012. doi:10.1007/978-3-642-23099-8.

[43] W. Kampinga, Y. H. Wijnant, A. de Boer, An efficient finite element model for viscothermal acoustics, Acta Acustica united with Acustica 97 (2011) 618–631.

[44] W. Kampinga, Y. Wijnant, A. de Boer, Performance of several viscothermal acoustic finite elements, Acta Acustica united with Acustica 96 (2010) 115–124.

[45] W. Bangerth, M. Geiger, R. Rannacher, Adaptive galerkin finite element methods for the wave equation, Computational Methods in Applied Mathematics 10 (2010) 3–48.

[46] J. W. Thomas, Numerical partial differential equations: finite difference methods, volume 22, Springer Science & Business Media, 2013.

[47] P. R. Amestoy, I. S. Duff, J. Koster, J.-Y. L'Excellent, A fully asynchronous multifrontal solver using distributed dynamic scheduling, SIAM Journal on Matrix Analysis and Applications 23 (2001) 15–41.

[48] T. Apel, T. Flaig, Crank–Nicolson schemes for optimal control problems with evolution equations, SIAM Journal on Numerical Analysis 50 (2012) 1484–1512.

[49] E. Jones, T. Oliphant, P. Peterson, et al., SciPy: Open source scientific tools for Python, 2001.

[50] P. Kungurtsev, Adjoint-based optimization for inkjet printing, Ph.D. thesis, University of Cambridge, 2021.